J. Fluid Mech. (1998), *vol.* 371, *pp.* 345–376. Printed in the United Kingdom

© 1998 Cambridge University Press

Gravity-driven creeping flow of two adjacent layers through a channel and down a plane wall

By C. POZRIKIDIS

University of California, San Diego, La Jolla, CA 92093-0411, USA
e-mail: costas@ames.ucsd.edu

(Received 26 February 1998 and in revised form 8 May 1998)

We study the stability of the interface between (*a*) two adjacent viscous layers flowing due to gravity through an inclined or vertical channel that is confined between two parallel plane walls, and (*b*) two superimposed liquid films flowing down an inclined or vertical plane wall, in the limit of Stokes flow. In the case of channel flow, linear stability analysis predicts that, when the fluids are stably stratified, the flow is neutrally stable when the surface tension vanishes and the channel is vertical, and stable otherwise. This behaviour contrasts with that of the gravity-driven flow of two superimposed films flowing down an inclined plane, where an instability has been identified when the viscosity of the fluid next to the plane is less than that of the top fluid, even in the absence of fluid inertia. We investigate the nonlinear stages of the motion subject to finite-amplitude two-dimensional perturbations by numerical simulations based on boundary-integral methods. In both cases of channel and film flow, the mathematical formulation results in integral equations for the unknown interface and free-surface velocity. The properties of the integral equation for multi-film flow are investigated with reference to the feasibility of computing a solution by the method of successive substitutions, and a deflation strategy that allows an iterative procedure is developed. In the case of channel flow, the numerical simulations show that disturbances of sufficiently large amplitude may cause permanent deformation in which the interface folds or develops elongated fingers. The ratio of the viscosities and densities of the two fluids plays an important role in determining the morphology of the emerging interfacial patterns. Comparing the numerical results with the predictions of a model based on the lubrication approximation shows that the simplified approach can only describe a limited range of motions. In the case of film flow down an inclined plane, we develop a method for extracting the properties of the normal modes, including the ratio of the amplitudes of the free-surface and interfacial waves and their relative phase lag, from the results of a numerical simulation for small deformations. The numerical procedure employs an adaptation of Prony's method for fitting a signal described by a time series to a sum of complex exponentials; in the present case, the signal is identified with the cosine or sine Fourier coefficients of the interface and free-surface waves. Numerical simulations of the nonlinear motion confirm that the deformability of the free surface is necessary for the growth of small-amplitude perturbations, and show that the morphology of the interfacial patterns developing subject to finite-amplitude perturbations is qualitatively similar to that for channel flow.

https://doi.org/10.1017/S0022112098002213 Published online by Cambridge University Press

1. Introduction

The stability of multi-layer channel flow and multi-film flow down a plane has been the object of a number of theoretical and experimental studies following the pioneering work of Yih (1967). Many of these studies have been motivated by a desire to understand manufacturing practice and improve on engineering design; multi-layer channel flows arise in industrial processes related to the manufacturing of laminated materials (Han 1981), and multi-film flows arise in the coating of photographic emulsions and magnetic suspensions (Kistler & Schweizer 1997). In both cases, a contrast in the viscosities of the layers or films may initiate instabilities and lead to two- or three-dimensional wavy patterns that are detrimental to the quality of the manufactured product.

Although a precise physical mechanism for the instability has been elusive, several observations that facilitate physical intuition have been made. Yiantsios & Higgins (1988) pointed out that a discontinuity in the shear rate across an interface, combined with inertial effects, is a prerequisite for the growth of small perturbations in two-layer Couette or Poiseuille flow. In Poiseuille flow, the shear rate may remain continuous across the interface even though the fluids may have different physical properties. Loewenherz & Lawrence (1989) identified instability in two-film flow down an inclined plane in the absence of fluid inertia. Chen (1993) emphasized that the free-surface deformability is necessary for the growth of small perturbations, and attributed the unstable behaviour to a resonance between the interface and free-surface waves. When the free surface is maintained flat by infinite surface tension, the instability does not appear. Three-layer channel flow and three-film flow down a plane have also been shown to be unstable in the limit of zero Reynolds number when the interfacial tensions are sufficiently small and the viscosity ratios lie within certain ranges (Li 1969; Weinstein & Kurz 1991). These results attest to the subtlety of the instability even under conditions of Stokes flow. A review of the literature, and numerical simulations of two-layer Couette or Poiseuille channel flow with finite-amplitude perturbations was presented by Pozrikidis (1997*c*). Reviews for film flow were presented by Chen (1992, 1993).

In the first part of this paper, §2, we consider the instability of two layers flowing through an inclined channel that is open at both ends, under conditions of Stokes flow and in the absence of a mean pressure gradient. The gravity-driven flow is an interesting hybrid of the shear- and pressure-driven flows, and provides us with a rich family of unidirectional base flows upon which a disturbance may grow or decay; the profile of the base flow is parametrized by the relative viscosities and densities of the two fluids. Linear stability analysis, to be discussed in §2, predicts that, in the limit of Stokes flow, and when the fluids are stably stratified, the flow is either stable or neutrally stable under any conditions. In the numerical investigations, we simulate the evolution of large-amplitude interfacial deformations using a boundary integral method for Stokes flow, and illustrate the precise role of the viscosity ratio and surface tension.

Tilley, Davis & Bankhoff (1994*a*, *b*) studied the instability of the two-layer flow in an inclined channel for a specified flow rate. When the flow rate is required to vanish, the channel is closed at both ends. In the first paper, these authors carried out a linear stability analysis for small-amplitude perturbations. In the second paper, they developed an asymptotic theory to describe the evolution of long waves, succeeded it by a weakly nonlinear analysis that produces a Kuramoto–Sivashinsky type of equation, and discussed the steepening of waves. Severtson & Aidun (1996) extended

https://doi.org/10.1017/S0022112098002213 Published online by Cambridge University Press

the linear stability analysis to the case of combined Couette–Poiseuille flow. In Appendix A of this paper, we develop a lubrication-flow model which is the counterpart of that arising from the first-order expansion of Tilley *et al.* (1994*b*), with variations due to differences in the global constraints. Comparing the results of numerical simulations obtained by the lubrication approximation to those obtained by the boundary-integral method allows us to assess the physical relevance of the simplified approach.

In the second part of this paper, §3, we consider the instability of the two-film Stokes flow down an inclined plane. The problem has been discussed by several previous authors with emphasis on the destabilizing effect of viscosity stratification, and the distinction between the free-surface and interface unstable modes. The former emphasizes the growth of the free surface, and the latter emphasizes the growth of the interface. In an unpublished series of reports, C. Kobayashi & L. E. Scriven (1981, 1982 Spring AIChE Meeting) and C. Kobayashi, K. Nohjo, N. Chino, Y. Yoshimura (1986 Spring AIChE Meeting) formulated and solved, by a Galerkin finite-element method, the linear stability problem for temporally and spatially growing perturbations, and compared their results to laboratory observations on a slide coating apparatus (Kobayashi 1992, 1995). Their results demonstrated that the flow can be unstable even at vanishing Reynolds number.

Loewenherz & Lawrence (1989) formulated and tackled the linear stability problem analytically for fluids of equal density, in the absence of interfacial and free-surface tension, and in the limit of Stokes flow. Their results showed explicitly that two-film flow can be unstable when the less-viscous fluid is adjacent to the wall. Their work was extended by Weinstein (1990) and Chen (1992) to non-Newtonian fluids and non-zero Reynolds numbers, and by Chen (1993) to a broader range of relative film thickness, non-zero surface tension, and non-zero Reynolds numbers. Evolution equations for perturbations of long wavelength based on lubrication models were derived and discussed by Kliahkhander & Sivashinsky (1997), In §3, we perform simulations of two-film flow with large-amplitude interfacial deformations using a boundary-integral method. The main objective is to compare the nature of the perturbed interfacial shapes to those developing from the instability of the two-layer channel flow.

One reason for studying multi-layer and the multi-film flows together, is that they both reduce to single-film flow down an inclined plane in special limits. In the case of channel flow, single-film flow emerges when the density and viscosity of one of the layers are negligible compared to those of the other layer. In the case of two-film flow, single-film flow emerges when the thickness of the upper film vanishes, or else the physical properties of the two fluids are equal and the interfaces have identical tensions. In spite of this similarity, channel flow is stable in the limit of Stokes flow, whereas film flow is unstable when the viscosity of the upper fluid is higher than that of the fluid next to the wall, as discussed in the previous paragraphs. The stability of single-film flow has been discussed by a number of authors following the seminal work of Yih (1963). A review was given by Chang (1994).

To carry out the numerical simulations, we develop two separate boundary-integral formulations, one for channel and the second for multi-film flow. These separate formulations allow us to obtain most accurate results with the least expense in computational time. In the case of multi-film flow, we study the properties of the Fredholm integral equation for the interface and free-surface velocities, and find them to be somewhat different from those of integral equations for flows with a single interface or multiple interfaces separating the same fluids. Knowledge of the eigenvalue spectrum allows us to deflate the double-layer operator and compute solutions by the

https://doi.org/10.1017/S0022112098002213 Published online by Cambridge University Press

method of successive substitutions. A desire to study the growth of unstable normal modes leads us to develop an apparently novel method for extracting them from the results of a numerical simulation with small deformations, based on Prony's method of exponential fitting. The method has a more general applicability and is suitable for studies of linear stability in a broader context, as will be discussed in the concluding section.

2. Two-layer flow in a channel

Consider the gravity-driven flow of two stratified fluids in a channel that is confined between two parallel plane walls located at $y = \pm H$. The channel is exposed to a constant-pressure ambient at both ends, and is inclined at an angle θ_0 with respect to the horizontal, as shown in figure 1(*a*). The lower and upper fluids are designated, respectively, with the superscript or subscript 1 and 2.

2.1. *Unidirectional flow*

In the simplest possible configuration, the interface is flat, located at $y = Y$, and the flow within both layers is unidirectional, directed along the x-axis. To derive expressions for the streamwise velocity profile $u_x(y)$, we require that the velocity vanish at the two walls, and the velocity and shear stress remain continuous across the interface. Using elementary methods, we find

$$u_x^{ud,1} = -\frac{\rho_1 g \sin\theta_0}{2\mu_1}(y-Y)^2 + \xi_1(y-Y) + u_x^{ud,I} \tag{2.1a}$$

and

$$u_x^{ud,2} = -\frac{\rho_2 \sin\theta_0}{2\mu_2}(y-Y)^2 + \xi_2(y-Y) + u_x^{ud,I}, \tag{2.1b}$$

where the superscript *ud* stands for *unidirectional* flow, ρ_1, μ_1 are the density and viscosity of the lower fluid, ρ_2, μ_2 are the density and viscosity of the upper fluid, and g is the magnitude of the acceleration due to gravity. The constant

$$\xi_1 = \frac{\rho_1 g H \sin\theta_0}{\mu_1}\frac{1}{1+R}\frac{\lambda-\beta R^2}{\lambda+R} \tag{2.2a}$$

is the shear rate in fluid 1 evaluated at the interface, $\lambda = \mu_2/\mu_1$ is the viscosity ratio, $\beta = \rho_2/\rho_1$ is the density ratio, and $R = H_2/H_1$ is the ratio of the layer thicknesses. Continuity of shear stress demands that the shear rate of fluid 2 at the interface be

$$\xi_2 = \xi_1/\lambda. \tag{2.2b}$$

The interfacial velocity is found to be

$$u_x^{ud,I} = \frac{\rho_1 g H^2 \sin\theta_0}{\mu_1}\frac{1+\beta R}{(1+R)^2}\frac{2R}{\lambda+R}. \tag{2.3}$$

The pressure fields corresponding to the velocity profiles (2.1*a*, *b*) are

$$p^{ud,1} = P_I + \rho_1 g\cos\theta_0(y-Y), \quad p^{ud,2} = P_I + \rho_2 g\cos\theta_0(y-Y), \tag{2.4a, b}$$

where P_I is the unspecified pressure at the interface.

Composite velocity profiles for layers of equal thicknesses, $R = 1$, and various combinations of λ and β are drawn in figure 1(*b*, *c*). Figure 1(*b*) shows the effect of β for fixed viscosity ratio $\lambda = 1$; when $\beta = 1$, we obtain parabolic flow with a symmetric

https://doi.org/10.1017/S0022112098002213 Published online by Cambridge University Press

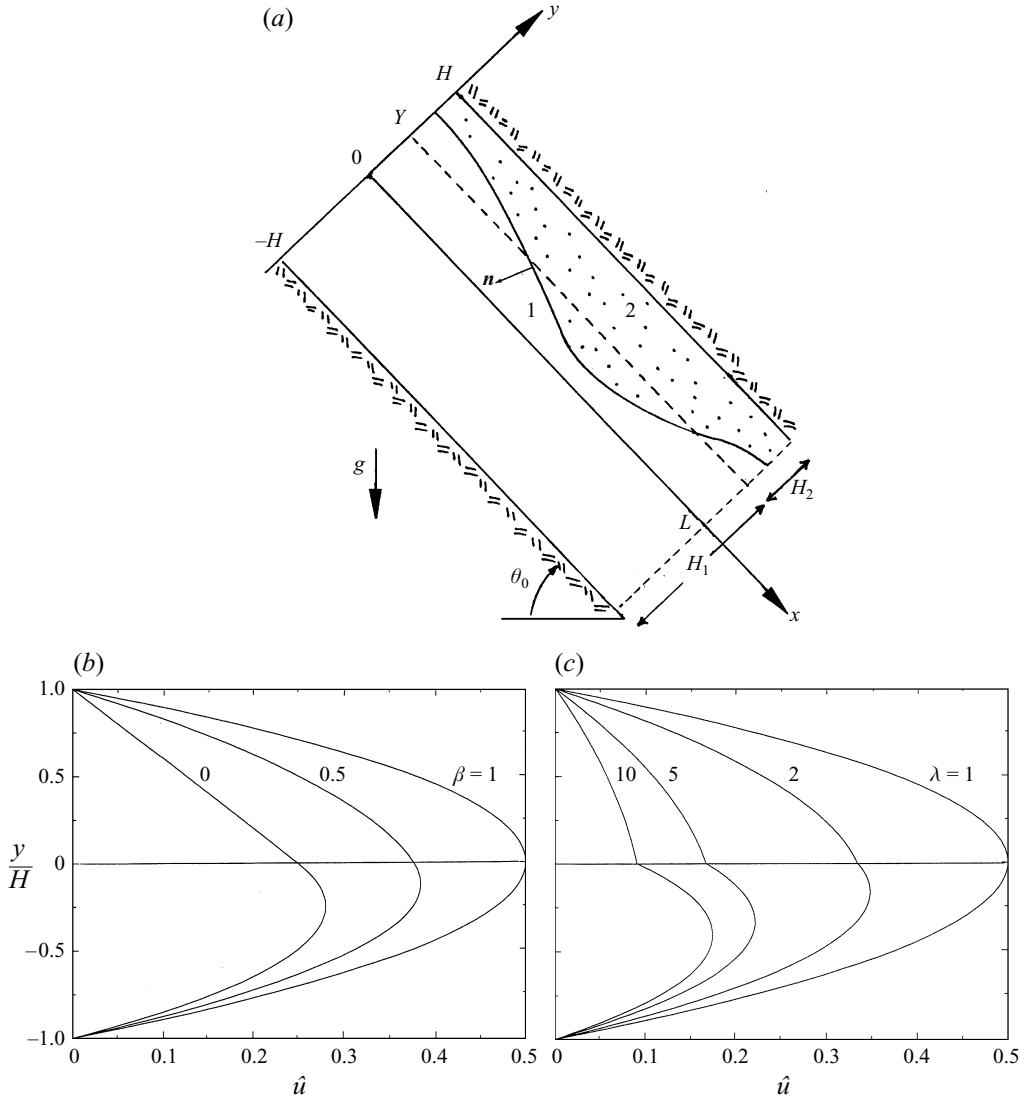


FIGURE 1. (*a*) Schematic illustration of gravity-driven flow of two layers through a channel confined between two parallel plates inclined at an angle θ_0 with respect to the horizontal; the dashed line shows the location of the unperturbed interface. (*b*) Composite profiles of the reduced velocity $\hat{u}_x \equiv u_x \mu_1/(\rho_1 g H^2 \sin\theta_0)$ for unidirectional flow with viscosity ratio $\lambda = \mu_2/\mu_1 = 1$ and density ratio $\beta = \rho_2/\rho_1 = 1$, 0.5, 0. (*c*) Composite velocity profiles for unidirectional flow with $\beta = 1$ and $\lambda = 1$, 2, 5, 10.

velocity profile; decreasing the density of the upper fluid, and thus the value of β, reduces the parabolicity of the velocity profile within it; when $\beta = 0$, the upper fluid executes simple shear flow driven by the interfacial velocity. Figure 1(*c*) shows the effect of the viscosity ratio λ for fixed density ratio $\beta = 1$, which is identical to pressure-driven flow in a channel with pressure gradient $-\mathrm{d}P/\mathrm{d}x = \rho_1 g \sin\theta_0$. When $\lambda = 1$, we obtain parabolic flow with a symmetric velocity profile; as the viscosity of the upper fluid and thus the value of λ is raised, the interfacial velocity is reduced; in the limit as λ tends to infinity, the interfacial velocity vanishes and the upper fluid becomes stationary.

https://doi.org/10.1017/S0022112098002213 Published online by Cambridge University Press

2.2. *Linear waves*

Next, we consider the motion of the interface subject to a two-dimensional periodic perturbation that disturbs the interface in a sinusoidal fashion with amplitude A_0 and wavelength L. Since the channel is exposed to a constant-pressure ambient at both ends, the perturbation is not allowed to generate a net pressure drop over each period. The behaviour of the linear wave is affected by seven dimensionless parameters including: the unperturbed layer thickness ratio $R = H_2/H_1$, the channel inclination angle θ_0, the viscosity ratio λ, the density ratio β, the capillary number $Ca = \rho_1 g H^2 \sin\theta_0/(2\gamma)$, and the geometrical ratios L/H and A_0/H. As the channel tends to become horizontal – that is, as θ_0 tends to zero – the capillary number tends to vanish independently of the physical properties of the fluids, and this requires an alternative scaling. In this limit, the two parameters β and Ca merge to give a new dimensionless group expressed by the Bond number $Bo = \rho_1(1-\beta) g H^2/\gamma = 2(1-\beta)\, Ca/\sin\theta_0$.

Assuming that: (*a*) an appropriate Reynolds number of the flow is so small that the effects of fluid inertia can be neglected uniformly and the motion of both fluids is governed by the equations of Stokes flow, and (*b*) the amplitude ratios A_0/H and A_0/L are both infinitesimal, we linearize the kinematic and dynamic condition at the interface and find that the sinusoidal perturbation decays or amplifies depending on the channel inclination angle and on the magnitudes of the density ratio and capillary number. For example, when the channel is horizontal and the upper fluid is heavier than the lower fluid, $\beta > 1$, the interface is susceptible to the Rayleigh–Taylor instability at sufficiently large values of the capillary number. When the channel is vertical, the interfacial waves are stable for non-zero surface tension or finite capillary number, and neutrally stable for zero surface tension or infinite capillary number. More generally, the linear analysis shows that small-amplitude interfacial waves evolve such that the position of the interface is described by the equation

$$y = y_I(x,t) = Y + A(t)\cos(k(x - c_P t)), \tag{2.5}$$

where $k = 2\pi/L$ is the wavenumber, c_P is the phase velocity of the perturbation,

$$A(t) = A_0 \exp(\sigma_I t) \tag{2.6}$$

is the instantaneous amplitude of the perturbation, σ_I is the growth rate, and $A_0 \equiv A(t=0)$. Lengthy relations between c_P, σ_I and the aforementioned geometrical and physical parameters may be derived in closed form working in the standard fashion (e.g. Pozrikidis 1997*a*, Chap. 9). A FORTRAN program that evaluates c_P and σ_I is available from the author on request. Later in this Section, we shall compare the predictions of the linear theory with the results of numerical simulations for finite-amplitude perturbations.

2.3. *Boundary-integral formulation*

We are mainly interested in studying the evolution of finite-amplitude waves by numerical simulations based on boundary-integral methods. In a recent paper, Pozrikidis (1997*c*) showed that the interfacial velocity $\boldsymbol{u}$ satisfies the following Fredholm integral equation of the second kind:

$$u_j(\boldsymbol{x}_0) = \frac{1+\beta}{1+\lambda} u_j^{R(1)}(\boldsymbol{x}_0) - \frac{1}{4\pi\mu_1}\frac{2}{1+\lambda}\int_I (\Delta f_i - \Delta f_i^R)(\boldsymbol{x})\, G_{ij}^{1P-2W}(\boldsymbol{x},\boldsymbol{x}_0;\alpha=0)\, \mathrm{d}l(\boldsymbol{x})$$
$$+ \frac{1}{2\pi}\frac{1}{1+\lambda}\int_I^{PV} [(1-\lambda)\, u_i(\boldsymbol{x}) - (1-\beta)\, u_i^{R(1)}(\boldsymbol{x})]\, T_{ijk}^{1P-2W}(\boldsymbol{x},\boldsymbol{x}_0;\alpha=0)\, n_k(\boldsymbol{x})\, \mathrm{d}l(\boldsymbol{x}), \tag{2.7}$$

https://doi.org/10.1017/S0022112098002213 Published online by Cambridge University Press

where the point $\boldsymbol{x}_0$ is located at the interface, and the rest of the variables are defined as follows. The tensor $\boldsymbol{G}^{1P-2W}(\boldsymbol{x},\boldsymbol{x}_0;\alpha)$ is the periodic Green's function of two-dimensional Stokes flow in a channel, representing the velocity due to an array of point forces; the value $\alpha = 0$ signifies that the flow due to a periodic array of point forces does not generate a net pressure drop, $1P$ stands for *singly periodic*, and $2W$ stands for *two walls*; $\boldsymbol{T}^{1P-2W}(\boldsymbol{x},\boldsymbol{x}_0;\alpha)$ is the associated stress tensor. The first term and the double-layer integral on the right-hand side of equation (2.7) involve the reference velocity

$$\boldsymbol{u}^{R,1} = \frac{\rho_1 g \sin\theta_0}{2\mu_1}(H^2 - y^2)\,\boldsymbol{e}_x, \tag{2.8}$$

where $\boldsymbol{e}_x$ is the unit vector along the x-axis. The quantity $\Delta\boldsymbol{f}(\boldsymbol{x}) = \gamma\kappa\boldsymbol{n}$ is the jump in traction across the interface, and κ is the curvature of the trace of the interface in the (x,y)-plane. The quantity

$$\Delta\boldsymbol{f}^R = \Delta\rho g y \begin{bmatrix} n_x\cos\theta_0 - n_y\sin\theta_0 \\ -n_x\sin\theta_0 + n_y\cos\theta_0 \end{bmatrix} - (P_1 - P_2)\,\boldsymbol{n} \tag{2.9}$$

is the jump in traction across the interface of two properly defined reference flows for the lower and upper fluid, with P_1 and P_2 being two constants. Finally, $\boldsymbol{n}$ is the unit normal vector pointing into the fluid 1, I is one period of the interface, and PV signifies the principal value of the double-layer integral.

Two special limits are worth noting. First, when $\lambda = 1$ and $\beta = 1$, the double-layer integral on the right-hand side of (2.7) vanishes yielding a representation for the velocity in terms of a single-layer potential alone. Secondly, when $\lambda = 0$ and $\beta = 0$, we may introduce the disturbance interface velocity $\boldsymbol{u}^D \equiv \boldsymbol{u} - \boldsymbol{u}^{R(1)}$, and obtain the simplified integral equation

$$u_j^D(\boldsymbol{x}_0) = -\frac{1}{2\pi\mu_1}\int_I (\Delta f_i - \Delta f_i^R)(\boldsymbol{x})\, G_{ij}^{1P-2W}(\boldsymbol{x},\boldsymbol{x}_0;\alpha=0)\,\mathrm{d}l(\boldsymbol{x}) + \frac{1}{2\pi}\int_I^{PV} u_i^D(\boldsymbol{x})\, T_{ijk}^{1P-2W}(\boldsymbol{x},\boldsymbol{x}_0;\alpha=0)\, n_k(\boldsymbol{x})\,\mathrm{d}l(\boldsymbol{x}) \tag{2.10}$$

which describes the flow of a liquid film with a free surface down a horizontal or inclined plane wall coinciding with the lower wall. In this limit, however, the use of an alternative Green function for semi-infinite flow bounded by a plane wall is more appropriate as it expedites the numerical solution.

The integral equation of the second kind (2.7) was solved by the iterative method described by Pozrikidis (1997*c*). The change in the area of each layer due to numerical error through a complete simulation was less than 0.1 % of the initial value, and much less than that in most cases. In a typical simulation, each period of an interface was described by 32 to 80 marker points. The computational cost depends strongly on the number of marker points and flow conditions, as will be discussed in the following subsections, demanding from 1 to 60 hours of CPU time on a SUN SPARCstation 20.

2.4. *Numerical simulations*

It was mentioned earlier that, when the densities of the two layers are equal, $\beta = 1$, the flow behaves similarly to pressure-driven flow in a channel with pressure drop over each period equal to $-\Delta P/L = \rho_1 g\sin\theta_0$, provided that the perturbation is not

https://doi.org/10.1017/S0022112098002213 Published online by Cambridge University Press

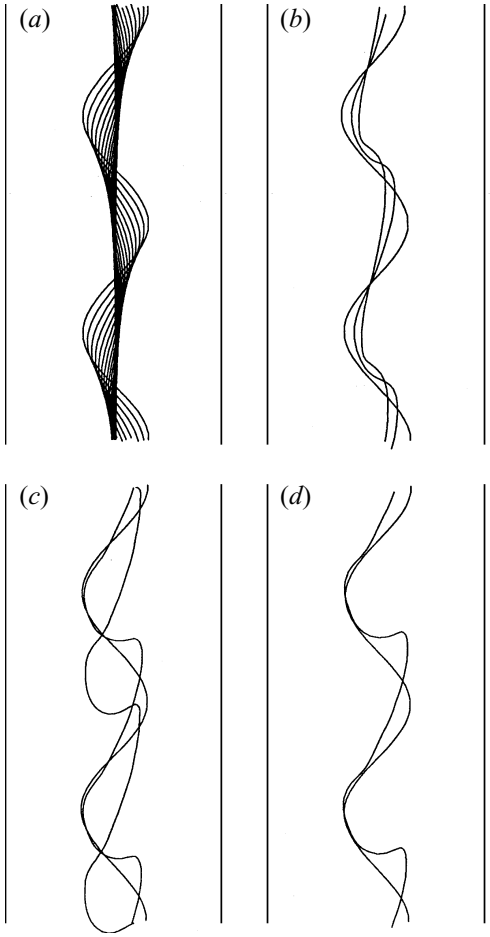


FIGURE 2(*a–d*). For caption see facing page.

allowed to generate a net pressure drop. The evolution of the interface subject to large-amplitude perturbations was studied by Pozrikidis (1997*c*). The results showed the existence of a critical reduced amplitude of the perturbation $(A_0/L)_{cr}$ below which the interfacial waves decay, and above which the interface suffers permanent deformation. The value of $(A_0/L)_{cr}$ depends on the magnitudes of the capillary number $Ca = \rho_1 g \sin\theta_0 H^2/(2\gamma)$ and viscosity ratio λ. Keeping A_0/L and Ca constant and increasing λ leads to permanent deformation.

Since the motion for $\beta = 1$ has been described, and since $\beta > 1$ corresponds to unstably stratified flow that lies beyond our scope, we consider flows with $\beta < 1$ and examine the effect of the capillary number. In figure 2(*a–d*), we present sequences of evolving interfacial profiles in a vertical channel, $\theta_0 = \frac{1}{2}\pi$, for $\beta = 0$, $\lambda = 1$, $L/H = 2$, $A_0/L = 0.15$ and $Ca = 0.5$, 5, 20, and ∞. For $Ca = 0.5$ and 5, the interfacial waves decay and the interface tends to become flat at long times; for $Ca = 20$, and ∞, a saw-tooth pattern develops with the dense fluid on the left attempting to penetrate the light fluid on the right. The computations were terminated when small-scale irregularities developed near the crests, possibly indicating the formation of wisps, and the motion could no longer be computed with a reasonable cost.

The behaviour of the waves is summarized in figure 2(*e*,*f*) where we display the

https://doi.org/10.1017/S0022112098002213 Published online by Cambridge University Press

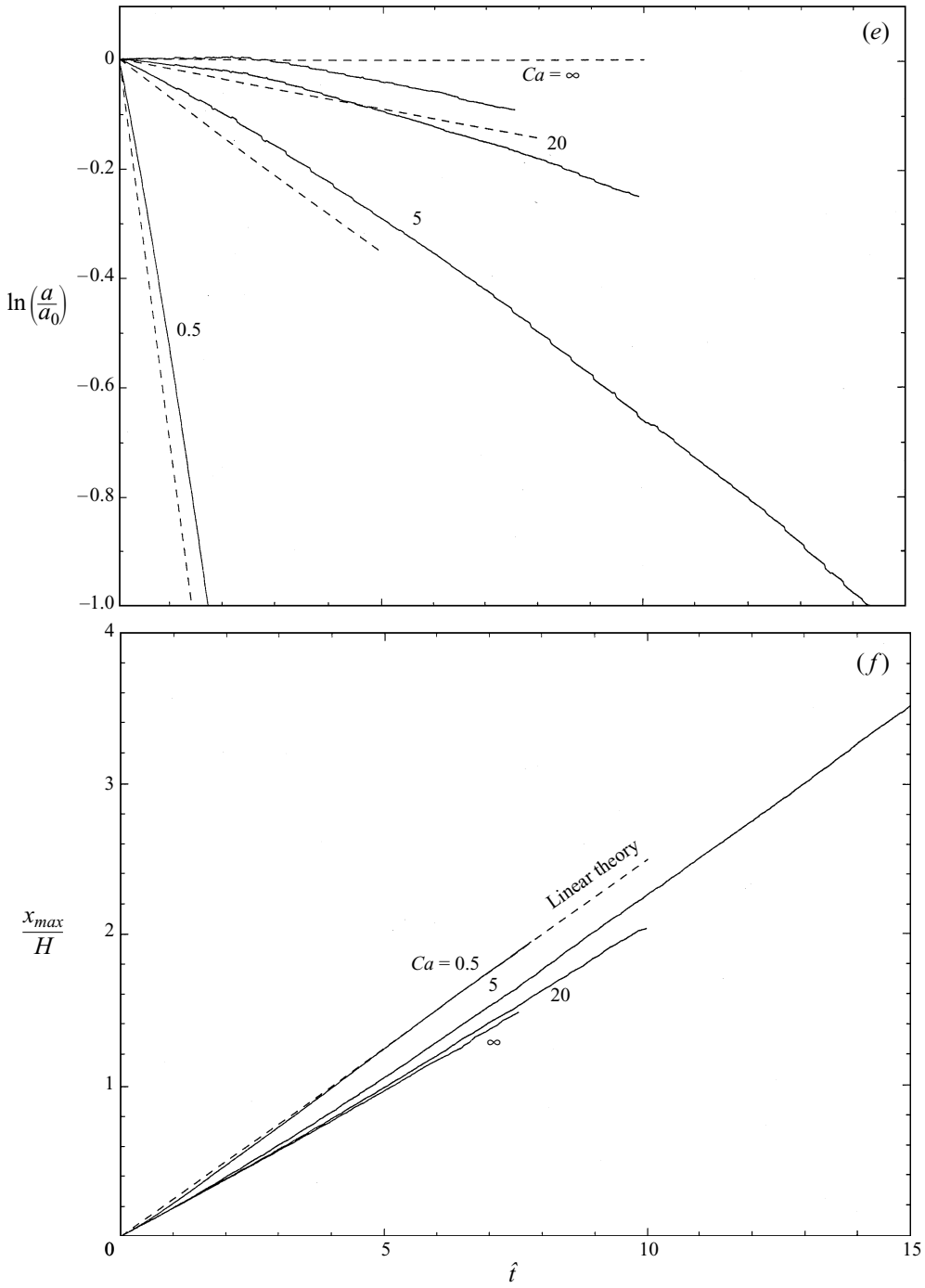


FIGURE 2. Effect of the capillary number on the stability of the two-layer channel flow. (*a–d*) Characteristic stages in the evolution of interfacial waves in a vertical channel, $\theta_0 = \frac{1}{2}\pi$, for density ratio $\beta = 0$, viscosity ratio $\lambda = 1$, reduced wavelength $L/H = 2$, reduced initial amplitude of the perturbation $A_0/L = 0.15$, for (*a*) $Ca = 0.5$, (*b*) 5, (*c*) 20, (*d*) ∞. (*e*) Evolution of maximum interfacial displacement from the unperturbed position with respect to dimensionless time $\hat{t} \equiv t\rho_1 gH/\mu_1$ and (*f*) *x*-location where the maximum occurs; the dashed lines represent the predictions of the linear theory.

https://doi.org/10.1017/S0022112098002213 Published online by Cambridge University Press

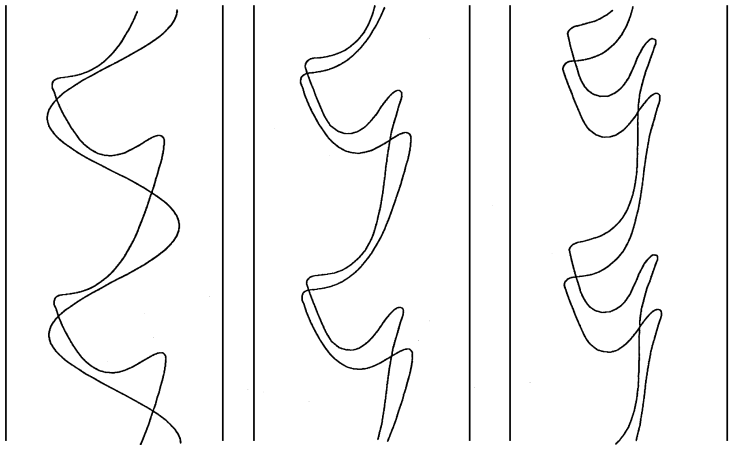


FIGURE 3. Effect of the disturbance amplitude on the stability of the two-layer channel flow. Characteristic stages in the evolution of interfacial waves in a vertical channel, $\theta_0 = \frac{1}{2}\pi$, for $\beta = 0$, $\lambda = 1$, $L/H = 2$, $A_0/L = 0.30$, and $Ca = 5$. Comparison with figure 2(*b*) shows that increasing the amplitude of the perturbation destabilizes the flow.

evolution of the maximum height of the interface a reduced by the initial amplitude $a_0 = A_0$, and the x-positions where the maximum occurs, x_{max}, for the four cases shown in figure 2(*a–d*). The dashed lines represent the analytical results of linear theory for small-amplitude waves, predicting that in the absence of surface tension, $Ca = \infty$, small-amplitude waves are neutrally stable. The numerical results in figure 2(*e*) show that finite-amplitude effects slow down the decay of the interfacial waves. For $Ca =$ 0.5, 5, the rate of decay at long times is close to that predicted by linear theory. Correspondingly, the phase velocity of the wave crests $\mathrm{d}x_{max}/\mathrm{d}t$ agrees well with that predicted by linear theory at small capillary numbers, but significant differences are observed at high capillary numbers.

To illustrate the effect of the amplitude of the perturbation, in figure 3 we present a sequence of interfacial profiles for $\theta_0 = \frac{1}{2}\pi$, $\beta = 0$, $\lambda = 1$, $L/H = 2$, $A_0/L = 0.3$, and $Ca = 5$. In this case, the interface does not recover the flat shape, as it did for $A_0/L = 0.15$, but develops a convoluted interfacial shape. We note, in particular, the curved shape near the left-hand wall where the velocity profile of the base flow is parabolic, and the finger-like shape near the right-hand wall where the velocity profile of the base flow is linear due to the vanishing density of the fluid on the right. It is clear that there is a critical amplitude of the perturbation, $A_{0,cr}$, above which the interface does not recover the flat shape.

A rough estimate for the critical amplitude may be derived by comparing the time it takes for the interfacial wave to decay according to linear theory, denoted by τ_D, and the time it takes for a pair of successive interfacial extrema to meet, having travelled a combined distance equal to $L/2$ under the action of the unperturbed flow, denoted by τ_T, thus generating a saw-tooth-like interfacial profile. Assuming that the amplitude of the wave has decayed in the value $0.1L$ after the time period τ_D, and using equation (2.6), we find $\tau_D \sigma_I = \ln(L/A_0) - 2.303$. The choice of the threshold amplitude $0.1L$ is significant only insofar as it indicates that the perturbation has become small compared to the wavelength; at that point, linear stability theory, predicting decay, will begin to be valid. To estimate τ_T, we note that the velocity at the crest of the upper fluid relative to the velocity at the trough of the lower fluid is equal to $\xi_1 A_0 + \xi_2 A_0$, where the shear rates ξ_1 and ξ_2 are given in equations (2.2*a*, *b*). Accordingly, we set

https://doi.org/10.1017/S0022112098002213 Published online by Cambridge University Press

$\tau_T = L/[2(\xi_1+\xi_2)\,A_0]$, assume that the interface will fold when $\tau_D > \tau_T$, and derive the following nonlinear algebraic equation for the critical amplitude:

$$\ln\frac{L}{A_{0,cr}} - \frac{\sigma_I}{2(\xi_1+\xi_2)}\frac{L}{A_{0,cr}} - 2.303 = 0. \tag{2.11}$$

Using the values $\xi_1 = \xi_2 = 0.25\rho_1 gH\sin\theta_0/\mu_1$ and $\sigma_1\mu_1/(\rho_1 gH\sin\theta_0) = -0.354/Ca$, the latter provided by linear stability theory, we find $A_{0,cr}/L = 0.72$, 0.20, 0.13, 0.10, respectively, for $Ca = 0.5$, 5, 20 and ∞. These critical values are consistent with the results of the simulations.

Next, we consider the effect of the viscosity ratio λ keeping all other parameters constant. It was mentioned earlier that when $\beta = 0$ and $\lambda = 0$, the layer flow reduces to single-film flow down an inclined plane. To study this limit, we developed an alternative boundary-integral formulation that is applicable in the more general case of multi-film flow, and will be described in §3 and Appendix B. This alternative formulation employs the Green's function of Stokes flow for semi-infinite flow bounded by a plane wall, which is much less expensive to compute than the Green's function for channel flow.

In figure 4(*a–c*), we present sequences of evolving interfacial profiles for a vertical channel, $\theta_0 = \frac{1}{2}\pi$, with $\beta = 0$, $\lambda = 0$, 0.1 and 10, $L/H = 2$, $A_0/L = 0.15$, and $Ca = 5$; when $\lambda = 0.1$, the fluid on the left is ten times more viscous than the fluid on the right. The evolution for $\lambda = 1$ was depicted in figure 2(*b*). First, we observe that when $\lambda = 0$, 0.1, the flat part of the interface slopes down to the right, whereas when $\lambda = 1$, 10 it slopes down to the left. The qualitative features of the motion for $\lambda = 0$ is consistent with that described by Gwynllyw & Peregrine (1996) using a different numerical method. Secondly, when $\lambda = 0$, 0.1 and 1, the interfacial waves decay and the interface tends to become flat at long times, whereas $\lambda = 10$, corrugations of nearly permanent form develop at long times. Thus, increasing the viscosity ratio, while keeping all other parameters constant, has a destabilizing influence on finite-amplitude perturbations. More direct evidence for this behaviour is offered in figure 4(*d*, *e*), showing the evolution of the reduced amplitude a/a_0 and the corresponding x-position. The predictions of the linear theory, represented by the dashed line, provide us with a fair description of the early stages of the motion for the large-amplitude perturbations.

To explain the permanent deformation of the interface with increasing λ, we offer two arguments. First, we introduce the alternative capillary number

$$Ca' \equiv \frac{\mu_1\xi_1 H_1}{\gamma} = \frac{1}{R}\frac{\mu_2\xi_2 H_2}{\gamma} = Ca\left(\frac{2}{1+R}\right)^2\frac{\lambda-\beta R^2}{\lambda+R} \tag{2.12}$$

which is defined with respect to the shear stress at the location of the unperturbed interface. For the conditions considered here, $\beta = 0$, $\lambda = 0$, 0.1, 1, 10 and $Ca = 0.10$ correspond, respectively, to $Ca' = 0$, 0.455, 0.250, 4.545. The increasing magnitude of Ca' with λ explains the occurrence of the instability. Secondly, we use equation (2.11) to estimate the critical amplitude, and find $A_{0,cr}/L = 0.68$, 0.20, 0.10 for $\lambda = 0.1$, 1, 10, consistent with the results of the simulations.

2.5. *Lubrication flow*

In Appendix A, we formulate a simplified theory that describes the evolution of interfacial waves whose period is long compared to the channel width, corresponding

https://doi.org/10.1017/S0022112098002213 Published online by Cambridge University Press

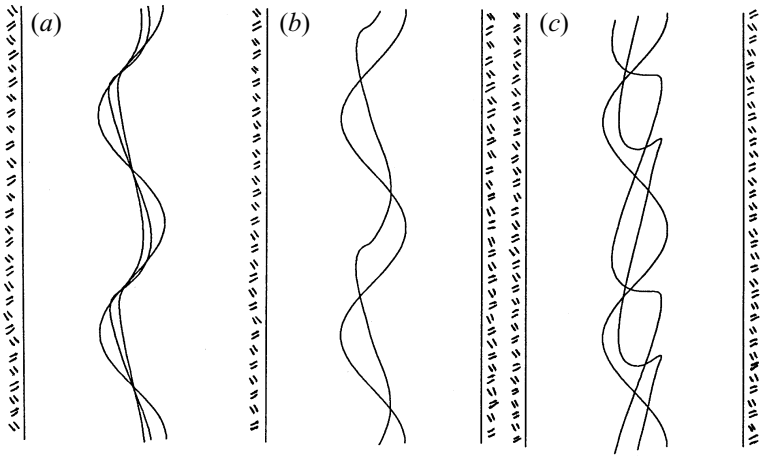


FIGURE 4(*a–c*). For caption see facing page.

to the leading-order small-wavenumber asymptotic expansion. The outcome of this theory is a highly nonlinear partial differential equation in x and t for the position of the interface. The equation is solved by a finite-difference method. The lubrication-flow model is expected to produce reliable results as long as the characteristic size of the interfacial patterns is large compared to half the channel width H. This requires that the interface can be described in terms of a single-valued function of x, and the slope of this function is small compared to unity at any point. Interfacial folding cannot be captured, but is suggested by the continued steepening of the interfacial profiles leading to discontinuous shapes.

To investigate the effectiveness of the simplified approach, we compare the results of numerical simulations conducted on the basis of it, with the results of simulations based on the boundary-integral method. In figure 5(*a–c*), we present sequences of evolving profiles for $\theta_0 = \frac{1}{2}\pi$, $\beta = 0$, $\lambda = 10$, $L/H = 2$, and $A_0/L = 0.15$, computed by the finite-difference methods discussed in Appendix A, all with 64 subdivisions over each wavelength. Figure 5(*a*) shows results for $Ca = 5$ obtained by the implicit centred-difference method. The explicit method requires an exceedingly small time step to suppress numerical instabilities due to the interfacial tension. Comparing the developing profiles to those shown in figure 4(*c*) reveals that the lubrication-flow model does not describe the unstable behaviour at this moderate wavenumber. Figure 5(*b*) displays results for $Ca = \infty$ obtained by the explicit centred-difference method, showing the development of saw-tooth-type waves familiar from figure 4(*c*). Numerical instabilities set in when the interfacial waves become steep, suggesting interface folding. The oscillations disappear when the centred-difference method is replaced by an upwind-differencing method, and the interface returns to the flat shape as shown in figure 5(*c*). This, however, only serves to warn us that numerical diffusivity may drastically alter the nature of a problem under consideration. Similar results are obtained for longer wavelengths, as shown in figure 5(*d–f*) for $\theta_0 = \frac{1}{2}\pi$, $\beta = 0$, $\lambda = 10$, $L/H = 6$, and $A_0/L = 0.05$.

Overall, the lubrication flow model emerges as a useful tool for assessing the qualitative features of the motion, even for moderate-wavelength perturbations and up to the point where parts of the interface becomes steep.

https://doi.org/10.1017/S0022112098002213 Published online by Cambridge University Press

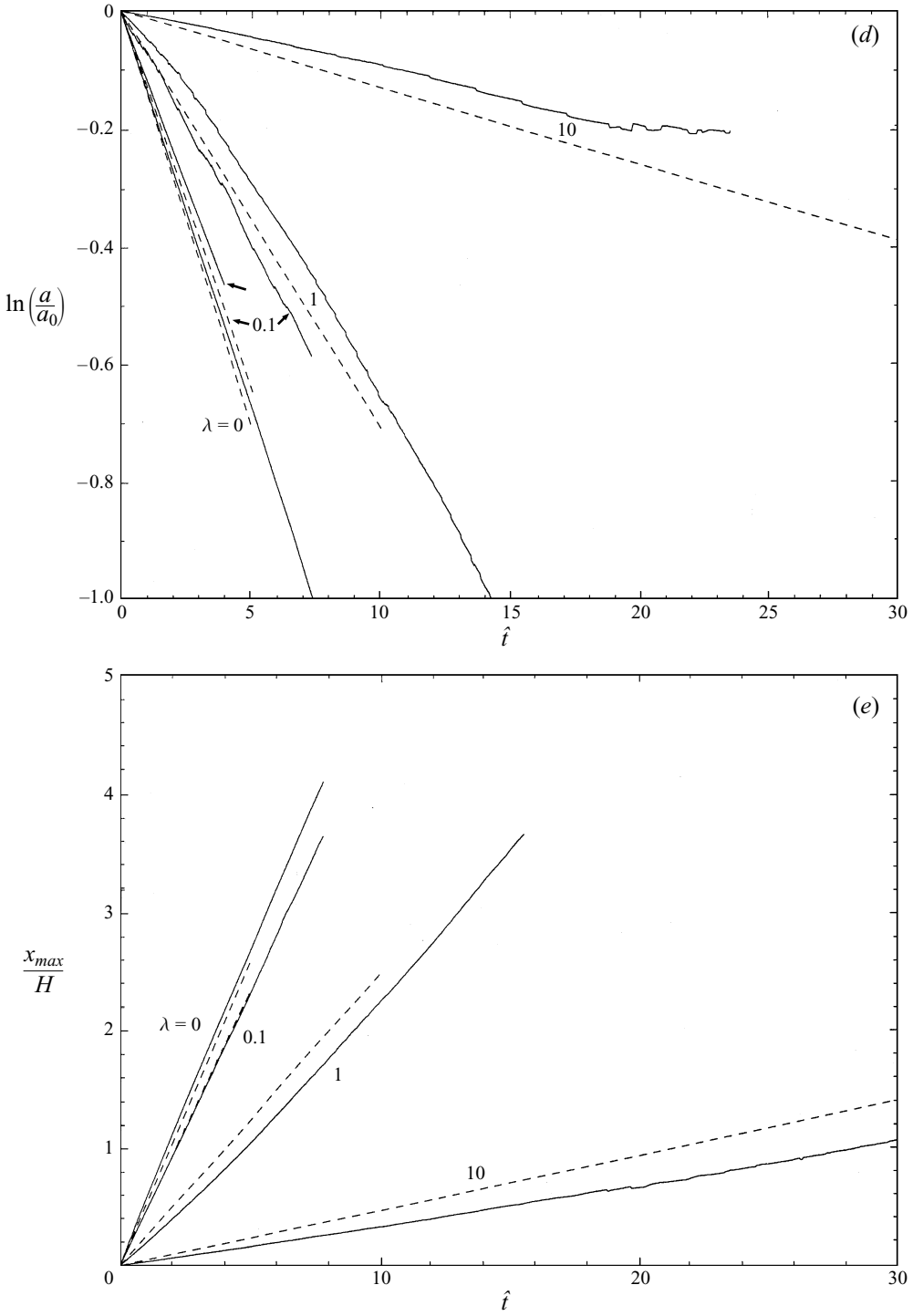


FIGURE 4. Effect of the viscosity ratio on the stability of the two-layer channel flow. Characteristic stages in the evolution of interfacial waves for a vertical channel, $\theta_0 = \frac{1}{2}\pi$, for $\beta = 0$, $L/H = 2$, $A_0/L = 0.15$, $Ca = 5$, and (*a*) $\lambda = 0$, (*b*) 0.1, (*c*) 10. (*d*) Evolution of the maximum interfacial displacement from the unperturbed position, and (*e*) x-location where the maximum occurs with respect to dimensionless time $\hat{t} \equiv t\rho_1 gH/\mu_1$; the dashed lines represent the predictions of the linear theory for small-amplitude waves. The line indicated by an arrow in (*d*) corresponds to $\lambda = 0.1$, and $A_0/L = 0.05$, included to confirm agreement with linear theory.

https://doi.org/10.1017/S0022112098002213 Published online by Cambridge University Press

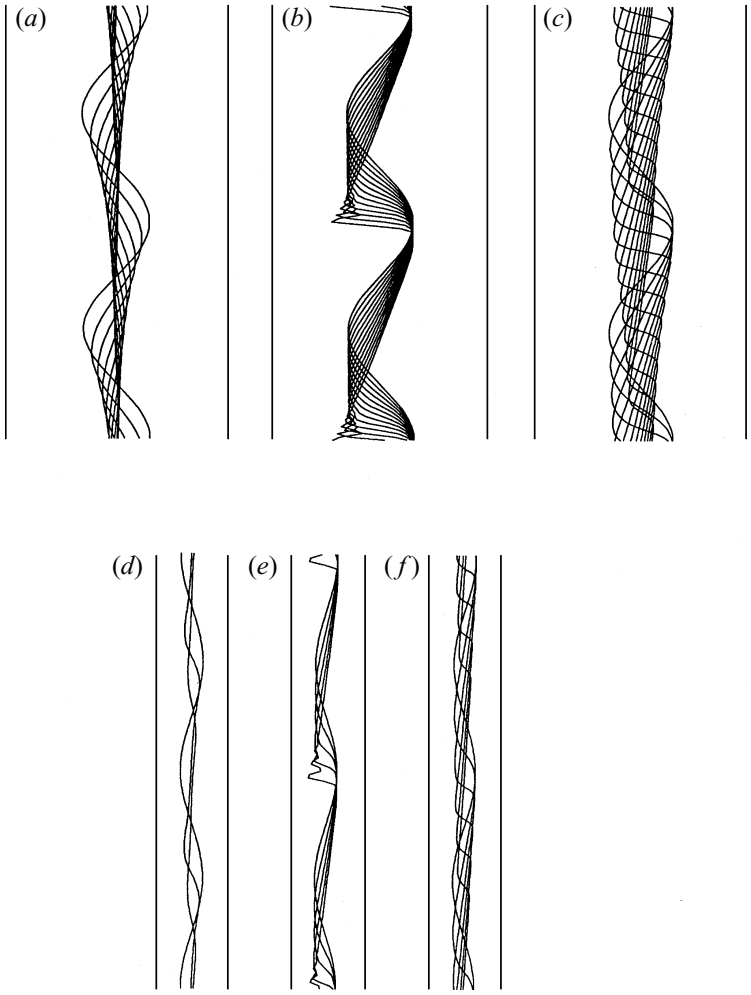


FIGURE 5. Evolution predicted by a simplified model based on the lubrication approximation. (*a–c*) Stages in the evolution of interfacial waves in a vertical channel, $\theta_0 = \frac{1}{2}\pi$, for $\beta = 0$, $L/H = 2$, $A_0/L = 0.15$, and $\lambda = 10$: (*a*) $Ca = 5$, evolution computed by the implicit centred-difference method; (*b*) $Ca = \infty$, evolution computed by the explicit centred-difference method; (*c*) $Ca = \infty$, evolution computed by the explicit upwind differencing method. (*d–f*) Same as in (*a–c*), but for a longer wave with $L/H = 6$, and $A_0/L = 0.05$.

3. Two-film flow down an inclined plane

We turn now to considering the gravity-driven flow of two superimposed films down an inclined plane, which is the second member of the inclusive family of multi-film flows with N superimposed films depicted in figure 6. The lower and upper fluids are labelled, respectively, with the subscript 1 and 2. Correspondingly, the interface and free surface are labelled, respectively, with the subscript 1 and 2.

3.1. *Unidirectional flow*

In the unperturbed state, the interface and free surface are both flat, located at $y = Y_1$ or Y_2, and the flow within each film is unidirectional along the x-axis. To derive expressions for the streamwise velocity profile $u_x(y)$, we require that the velocity vanish

https://doi.org/10.1017/S0022112098002213 Published online by Cambridge University Press

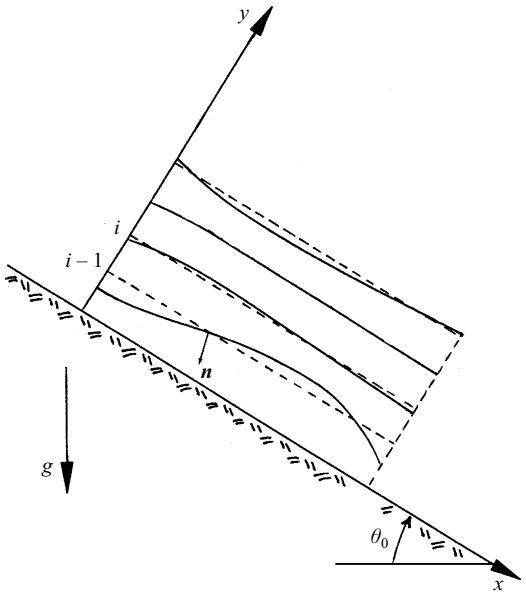


FIGURE 6. Schematic illustration of gravity-driven flow of N superimposed films down a plane wall inclined at an angle θ_0 with respect to the horizontal. The dashed horizontal lines show the positions of the unperturbed interfaces and of the free surface. The normal vector at the ith interface points into the ith film which is confined between the interfaces numbered i and $i-1$; the zeroth interface is the plane wall.

at the wall, the velocity and shear stress be continuous across the interface, and the shear stress vanish at the free surface. Using elementary methods, we derive the expressions

$$u_x^{ud,1} = \frac{\rho_1 g \sin\theta_0}{2\mu_1} y(2H_1 + 2\beta H_2 - y), \tag{3.1a}$$

$$u_x^{ud,2} = \frac{\rho_2 g \sin\theta_0}{2\mu_2}\left(\frac{\lambda}{\beta}H_1^2 + 2\lambda H_1 H_2 - H_1(2H_2 - H_1) + 2(H_1 + H_2)\, y - y^2\right), \tag{3.1b}$$

where, as in §2, *ud* stands for *unidirectional* flow, $\lambda = \mu_2/\mu_1$ is the viscosity ratio, $\beta = \rho_2/\rho_1$ is the density ratio, and H_1, H_2 are the uniform film thicknesses. When (*a*) $\beta = 1$ and $\lambda = 1$, or (*b*) one of the film thicknesses H_1, H_2 vanishes, we recover the single-film flow.

It is worth noting that the velocity profile across the film next to the wall is independent of the viscosity of the upper film. This can be explained by writing a macroscopic force balance for the two-film system, and then using the condition of zero shear stress at the free surface to show that the wall shear stress is determined by the densities of the two fluids. Observing that the velocity profile within the wall film is determined by its kinematic viscosity and the value of the wall shear stress, explains the aforementioned independence on μ_2. A similar argument can be made for multi-film flow.

3.2. *Linear interfacial waves*

Next, we consider the motion subject to a two-dimensional periodic perturbation with wavelength L that disturbs the interface and free surface in a sinusoidal fashion with different amplitudes and an arbitrary phase lag. Assuming that the flow occurs under

https://doi.org/10.1017/S0022112098002213 Published online by Cambridge University Press

conditions of Stokes flow, and that each wave amplitude is small compared to L as well as to the unperturbed layer thicknesses, we linearize the kinematic and dynamic interfacial conditions and carry out a normal-mode stability analysis to find that exponentially growing or decaying interface and free-surface waves are described, respectively, by the equations

$$y = y_1(x,t) = Y_1 + A_1^{NM,l}(t)\cos\left(k(x - c_P^{NM,l}t)\right), \tag{3.2a}$$

$$y = y_2(x,t) = Y_2 + A_2^{NM,l}(t)\cos\left(k(x - c_P^{NM,l}t) - \Delta\phi_2^{NM,l}\right), \tag{3.2b}$$

where $k = 2\pi/L$ is the wavenumber, and $\Delta\phi_2^{NM,l}$ is the phase lag of the free-surface wave with respect to the interfacial wave for the lth normal mode; the superscript NM stands for *Normal Mode*. The amplitudes $A_1^{NM,l}(t)$ and $A_2^{NM,l}(t)$ are exponential functions of time given by

$$A_j^{NM,l}(t) = A_j^{NM,l}(t=0)\exp\left(\sigma_I^{NM,l}t\right) \tag{3.3}$$

for $j = 1, 2$. For each unperturbed layer configuration, there are two normal modes, designated by $l = 1, 2$. One of these modes, called the *interface mode* and identified by $l = 1$, may be unstable, whereas the second mode, called the *free-surface mode* and identified by $l = 2$, is stable in the limit of Stokes flow.

A complete description of the lth normal mode requires the specification of the following properties: (*a*) the constant ratio of the amplitudes of the free-surface and interface waves, $r_2^{NM,l} \equiv A_2^{NM,l}(t)/A_1^{NM,l}(t)$, (*b*) the phase lag $\Delta\phi_2^{NM,l}$, (*c*) the phase velocity $c_P^{NM,l}$, and (*d*) the growth rate $\sigma_I^{NM,l}$. Loewenherz & Lawrence (1989) and Chen (1993) presented graphs of selected properties of the interface mode as functions of several geometrical and physical dimensionless groups including the wavenumber. Loewenherz & Lawrence first pointed out that when the less-viscous fluid is next to the wall, and the surface tension is sufficiently small, the flow could be unstable. The properties of the stable free-surface mode have not been discussed in the limit of zero Reynolds number.

In investigations of nonlinear instability, it is desirable to specify an initial condition that corresponds to the most unstable normal mode. But since the complete properties of this mode are unavailable, we develop a method for extracting them from the results of a numerical simulation with small deformations. We begin by considering the motion when the interface and the free surface are perturbed by waves of arbitrary but sufficiently small amplitude and with an arbitrary phase lag. At the origin of time, the position of the interface and of the free surface is described by the equations

$$y = y_j(x, t=0) = Y_j + A_j\cos\left(kx - \phi_j\right) \tag{3.4}$$

for $j = 1, 2$. Normal-mode decomposition yields

$$y_j(x, t=0) = Y_j + \sum_{l=1}^{2} A_j^{NM,l}(t=0)\cos\left(kx - \phi_j^{NM,l}\right) \tag{3.5}$$

for $j = 1, 2$. The arguments of the trigonometric functions in equations (3.5) evolve according to equations (3.2*a*, *b*), and the amplitudes $A_j^{NM,l}(t)$ evolve according to equation (3.3). Combining these expressions, we derive evolution equations for arbitrary linear waves in terms of the properties of the normal modes:

$$y_j(x,t) = Y_j + \sum_{l=1}^{2} A_j^{NM,l}(t=0)\cos\left(k(x - c_P^{NM,l}t) - \phi_j^{NM,l}\right)\exp\left(\sigma_I^{NM,l}t\right) \tag{3.6}$$

for $j = 1, 2$.

https://doi.org/10.1017/S0022112098002213 Published online by Cambridge University Press

To compute the eight unknown constants $A_j^{NM,l}(t=0)$, $\phi_j^{NM,l}$, for $j, l = 1, 2$, we set the right-hand side of equation (3.5) equal to the right-hand side of (3.4), and require that the sums of coefficients of like trigonometric functions balance to zero; this provides us with a system of four algebraic-trigonometric equations. If the normal-mode wave amplitude ratios $r_2^{NM,l}$ and phase lags $\Delta\phi_2^{NM,l} \equiv \phi_2^{NM,l} - \phi_1^{NM,l}$ were available for $l = 1, 2$, we could have invoked their definitions to obtain an additional set of four equations, and this would raise the total number of unknowns to the number of the equations. Confronted with the unavailability of the properties of the normal modes, we express equation (3.6) in the form

$$y_j(x, t) = Y_j + F_{j,c}(t)\cos kx + F_{j,s}(t)\sin kx \tag{3.7}$$

involving the first-order cosine and sine coefficients of the complete Fourier series of the functions $y_j(x, t)$ with respect to x, defined as

$$F_{j,c}(t) = \sum_{l=1}^{2} A_j^{NM,l}(t=0)\cos(\sigma_R^{NM,l}t + \phi_j^{NM,l})\exp(\sigma_I^{NM,l}t), \tag{3.8a}$$

$$F_{j,s}(t) = \sum_{l=1}^{2} A_j^{NM,l}(t=0)\sin(\sigma_R^{NM,l}t + \phi_j^{NM,l})\exp(\sigma_I^{NM,l}t). \tag{3.8b}$$

We have introduced the complex growth rate $\sigma_R^{NM,l} = kc_P^{NM,l}$. The key idea is that the left-hand sides of equations (3.8*a*, *b*) may be expressed as sums of complex exponentials, and the eight real unknowns $A_j^{NM,l}(t=0)$, $\phi_j^{NM,l}$, $j, l = 1, 2$, may be recovered by performing N-mode complex exponential fitting using the method of Prony (e.g. Hildebrand 1974, pp. 457–463; Kay & Marple 1981; Marple 1987, pp. 303–349).

To implement the method, we write

$$F_{j,c}(t) = \frac{1}{2}\sum_{l=1}^{2}[c_{j,c}^{(l)}\exp(-\mathrm{i}\sigma^{NM,l}t) + c_{j,c}^{(l)*}\exp(\mathrm{i}\sigma^{NM,l*}t)], \tag{3.9a}$$

and

$$F_{j,s}(t) = \frac{1}{2}\sum_{l=1}^{2}[c_{j,s}^{(l)}\exp(-\mathrm{i}\sigma^{NM,l}t) + c_{j,s}^{(l)*}\exp(\mathrm{i}\sigma^{NM,l*}t)], \tag{3.9b}$$

where $\sigma^{NM,l} = \sigma_R^{NM,l} + \mathrm{i}\sigma_I^{NM,l}$ are the complex rates, i the imaginary unit, an asterisk designates the complex conjugate, and $c_{j,c}^{(l)}$, $c_{j,s}^{(l)}$, are complex coefficients. Setting the right-hand sides of (3.9*a*, *b*) equal to the right-hand sides of (3.8*a*, *b*), we obtain

$$c_{j,c}^{(l)} = A_j^{NM,l}(t=0)\exp(-\mathrm{i}\phi_j^{(l)}), \quad c_{j,s}^{(l)} = A_j^{NM,l}(t=0)\exp(-\mathrm{i}(\phi_j^{(l)} - \tfrac{1}{2}\pi)). \tag{3.10a, b}$$

Assume now that we have available an $(M+4)$-long time series for $F_{j,c}(t)$ with constant sampling time Δt, and denote, for brevity, $\zeta_q \equiv F_{j,c}(q\,\Delta t)$, where $q = 0, 1, 2, \ldots$. Prony's method proceeds in four stages. At the first stage, we solve the generally overdetermined $M \times 4$ linear system of equations

$$\begin{bmatrix} \zeta_1 & \zeta_2 & \zeta_3 & \zeta_4 \\ \zeta_2 & \zeta_3 & \zeta_4 & \zeta_5 \\ \cdots & \cdots & \cdots & \cdots \\ \zeta_M & \zeta_{M+1} & \zeta_{M+2} & \zeta_{M+3} \end{bmatrix} \begin{bmatrix} \alpha_4 \\ \alpha_3 \\ \alpha_2 \\ \alpha_1 \end{bmatrix} = - \begin{bmatrix} \zeta_5 \\ \zeta_6 \\ \vdots \\ \zeta_{M+4} \end{bmatrix} \tag{3.11}$$

https://doi.org/10.1017/S0022112098002213 Published online by Cambridge University Press

for the four real unknowns α_1, α_2, α_3, α_4, where $M \geqslant 4$. At the second stage, we compute the roots z_1, z_2, z_3, z_4 of the fourth-degree characteristic polynomial

$$P_4(z) = z^4 + \alpha_1 z^3 + \alpha_2 z^2 + \alpha_3 z + \alpha_4. \tag{3.12}$$

Since the coefficients of this polynomial are real, complex roots appear in two pairs of complex conjugates $(z_1, z_2 = z_1^*)$, $(z_3, z_4 = z_3^*)$. At the third stage, we extract the complex growth rates from the relations

$$z_1 = \exp(-\mathrm{i}\sigma^{NM,1}\Delta t), \quad z_2 = \exp(\mathrm{i}\sigma^{NM,1*}\Delta t), \tag{3.13a,b}$$

$$z_3 = \exp(-\mathrm{i}\sigma^{NM,2}\Delta t), \quad z_4 = \exp(\mathrm{i}\sigma^{NM,2*}\Delta t). \tag{3.13c,d}$$

Finally, we recover the coefficients $c_{j,c}^{(l)}$ by solving a generally overdetermined linear system of equations arising from (3.9a) using the computed values of $\sigma^{NM,1}$ and $\sigma^{NM,2}$, and recover $A_j^{NM,l}(t=0)$, $\phi_j^{(1)}$, $A_j^{NM,2}(t=0)$, $\phi_j^{(2)}$, from equations (3.10a,b).

There is an ambiguity in the definition of $\sigma^{NM,l}$, stemming from our freedom to freely interchange the complex conjugate roots z_1 and z_2 on the left-hand sides of equations (3.13a,b), which amounts to replacing $\sigma^{NM,1}$ with its complex conjugate on the right-hand side; similarly for equations (3.13c,d). To resolve this ambiguity, we also perform the Prony fitting of the sine coefficient $F_{j,s}(t)$ by introducing a time series for $F_{j,s}(t)$, setting $\zeta_q \equiv F_{j,s}(q\,\Delta t)$, and working in a similar fashion with (3.9b) in place of (3.9a), thereby recovering a quadruple of values $A_j^{NM,l}(t=0)$, $\phi_j^{(l)}$, $A_j^{NM,l}(t=0)$, $\phi_l^{(l)}$ for $j = 1, 2$. The proper values of $\sigma^{NM,l}$ are the ones giving the same – in numerical practice, nearly the same – values of $A_j^{NM,l}(t=0)$, $\phi_j^{(l)}$ computed from the fitting of $F_{j,c}(t)$ or $F_{j,s}(t)$. Combining the results for the interface and for the free surface allows us to deduce the wave amplitude ratio and phase lag of the normal modes.

3.3. *Numerical simulations*

To describe the evolution of finite-amplitude waves, we use the boundary-integral method for Stokes flow with multiple interfaces. In Appendix B, we present a boundary-integral formulation that is applicable to the general case of multi-film flow with an arbitrary number of films depicted in figure 6; we derive a Fredholm integral equation of the second kind for the interfacial and free-surface velocities; and we investigate the spectrum of eigenvalues of the double-layer operator. The integral equation is deflated and solved using an iterative method that is similar to the method described in §2 for two-layer channel flow.

In the numerical simulations, the initial position of the interface and free surface is described by equations (3.4). Ten dimensionless parameters affect the evolution of the flow: the unperturbed layer thickness ratio $R = H_2/H_1$, the plane inclination angle θ_0, the viscosity ratio $\lambda = \mu_2/\mu_1$, the density ratio $\beta = \rho_2/\rho_1$, the capillary numbers $Ca_1 = \rho_1 g H^2 \sin\theta_0/(2\gamma_1)$ and $Ca_2 = \rho_1 g H^2 \sin\theta_0/(2\gamma_2)$, the reduced wavelength L/H, the reduced amplitudes A_1/H and A_2/H, and the phase lag $\Delta\phi = \phi_2 - \phi_1$; $H = H_1 + H_2$ is the total layer thickness. Consistent with our main goal, which is to study the effect of the viscosity contrast, we set $\beta = 1$, but this still leaves us with a large parametric space that we explore by case-study investigations.

Consider a system with $\theta_0 = 0.06366\pi = 0.2$, $\lambda = 2.5$, $\beta = 1$, $Ca_1 = \infty$, and $Ca_2 = \infty$. Chen (1993, figure 4) presented graphs of the reduced growth rate of the unstable normal mode $\hat{\sigma}_L^{NM,1} \equiv \sigma_I^{NM,1} H_1/u^{ud,I}$ against the reduced wavenumber $\alpha = kH_1$, for several values of the layer thickness ratio R; $u^{ud,I}$ is the interfacial velocity. For $R = 0.5$ and $\alpha = 3.75$ or $L/H = 1.117$, his results show that $\hat{\sigma}_I^{NM,1} = 0.01625$. We

https://doi.org/10.1017/S0022112098002213 Published online by Cambridge University Press

note that $u^{ud,I} = 0.08830\ \rho_1 gH^2/\mu_1$, introduce the reduced growth rate $\hat{\sigma}_I^{NM,1} \equiv \sigma_I^{NM,1}\mu_1/(\rho_1 gH)$, and find $\hat{\sigma}_I^{NM,1} = 0.0022$.

First, we use Prony's method, implemented as described in §3.2, to extract the properties of the unstable normal mode. For this purpose, we introduce the complete Fourier series expansion of the space-periodic function $y_1(x,t)$ describing the position of the interface, and of the space-periodic function $y_2(x,t)$ describing the position of the free surface, both series with respect x, and truncate them at the fundamental frequency to obtain equation (3.7). In the numerical simulations, the interfaces are represented by a set of unevenly spaced marker points, typically on the order or 50, and values of the functions $y_1(x,t)$ and $y_2(x,t)$ are available at the marker point abscissas. The Fourier coefficients $F_{j,c}(t)$, $F_{j,s}(t)$ are retrieved from Fourier transform integrals evaluated by the 1/3 Simpson rule with overlapping parabolas (e.g. Pozrikidis 1998, Chap. 8). The overdetermined systems of equations for the polynomial coefficients and for the coefficients of the Prony expansion are solved by the normal-equation least-squares method followed by Cholesky decomposition (e.g. Pozrikidis 1998, Chap. 3).

In figure 7(*a*), we plot $F_{j,c}(t), F_{j,s}(t)$, for $A_1/H = 0.01$, $A_2/H = 0.005$, $\phi_1 = 0$, $\phi_2 = 0.75\pi$, and observe an initial adjustment period followed by growing oscillations. The symbols represent the results of Prony's method with sampling time $\Delta t = 1.5\mu_1/(\rho_1 gH)$. To assist the probing of the unstable normal mode, the Prony fitting of the sine coefficients $F_{j,s}(t)$ was done over the indicated time period, following an initial transient period where the amplitude of the stable normal mode has decayed leaving the unstable mode. The two-mode fitting of the Fourier coefficients yields values for $\hat{\sigma}_R^{NM,1} \equiv \sigma_R^{NM,1}\mu_1/(\rho_1 gH)$ in the range (0.494, 0.497), and for $\hat{\sigma}_I^{(1)}$ in the range $(0.0019, 0.0029)$ which contains the value 0.0022 predicted by linear theory. Furthermore, the results suggest that $r_2^{NM,1} \approx 7$ and $\Delta\phi_2^{NM,1} \approx 0.7\pi$.

It is important to note that the amplitude of the interface wave of the unstable normal mode is roughly seven times that of the free-surface wave, and this confirms that, under the conditions of Stokes flow considered here with $\lambda = 2.5$, $Ca_1 = \infty$, $Ca_2 = \infty$, the instability originates from the interface, with the deformability of the free surface acting as a controller. In practice, the smallness of the amplitude of the free surface compared to the amplitude of the interface, the smallness of the growth rate, and the observation that the flow is stable when the free surface is not deformable, explains why an accurate numerical method is required to reliably describe the evolution of the flow.

In figure 7(*b*), we plot the Fourier coefficients for a disturbance that nearly corresponds to the unstable normal mode, with $A_1/H = 0.035$, $A_2/H = 0.005$, $\phi_1 = 0$, $\phi_2 = 0.70\pi$, and observe an almost pure exponential growth. The one-mode Prony fitting yields values for $\hat{\sigma}_R^{(1)}$ and $\hat{\sigma}_I^{(1)}$ in the ranges stated in a previous paragraph. Three stages in the evolution of the flow, after the interfacial wave has grown to a large amplitude, are displayed in figure 7(*c*). The computation ended when small-scale irregularities developed near the inflection point of the overturning interface, possibly a precursor of local penetration or wisp formation. The interfacial profile at the last stage is qualitatively similar to that described in §2 for two-layer channel flow; the free-surface is remarkably flat.

Next, we consider the effect of interfacial tension γ_1 expressed by the first capillary number Ca_1, keeping $Ca_2 = \infty$. Linear stability analysis predicts that increasing γ_1 reduces the growth rate of an unstable perturbation, and eventually stabilizes the flow. As a test case, we consider a system with $\theta_0 = 0.06366\pi = 0.2$, $R = 0.75$, $\lambda = 2.5$, $\beta = 1$, $Ca_1 = 15.55$, and $Ca_2 = \infty$, and a perturbation with $L/H = 1.117$ or $\alpha = 3.21$, amplitudes $A_1/H = 0.030$, $A_2/H = 0.010$, and phases $\phi_1 = 0$, $\phi_2 = 0.25\pi$. In figure

https://doi.org/10.1017/S0022112098002213 Published online by Cambridge University Press

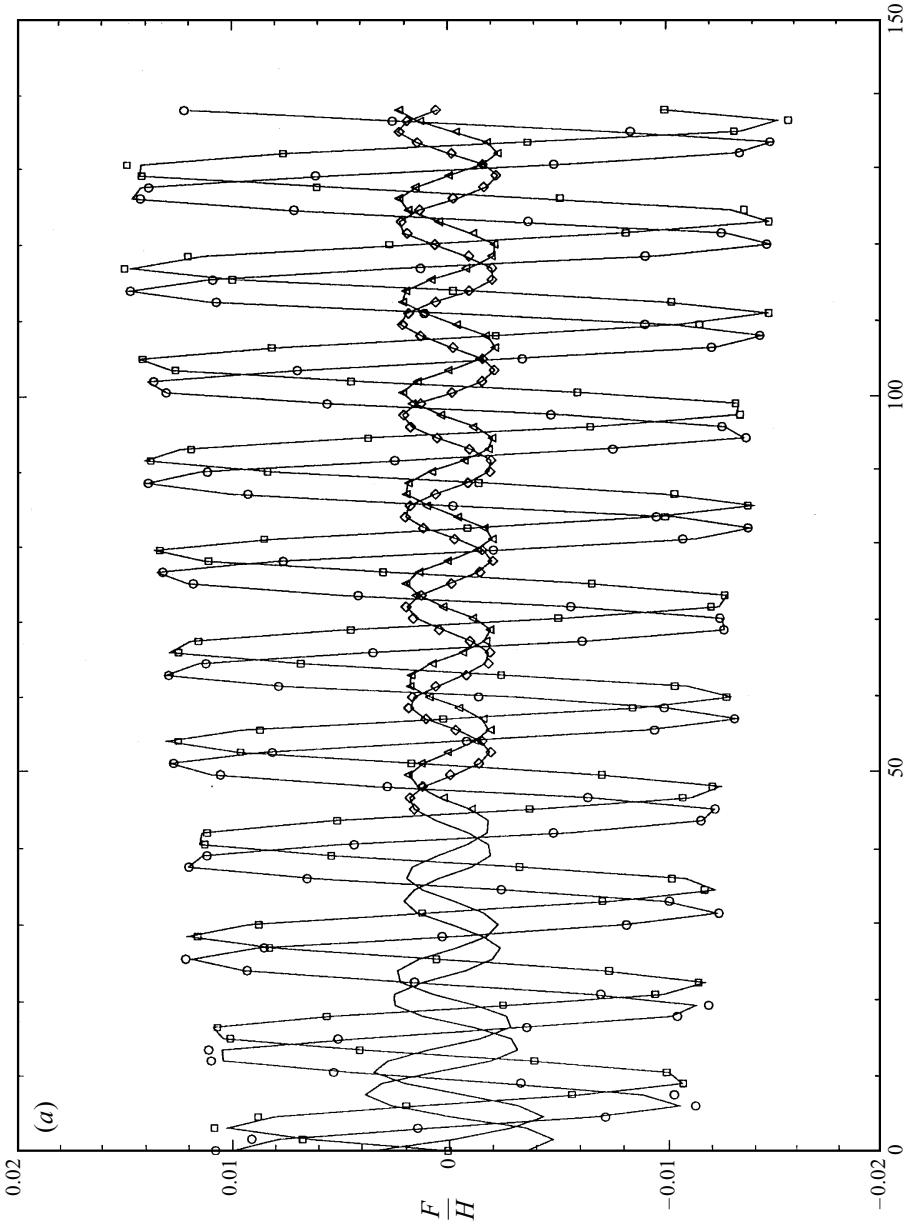


FIGURE 7(*a*). For caption see facing page.

https://doi.org/10.1017/S0022112098002213 Published online by Cambridge University Press

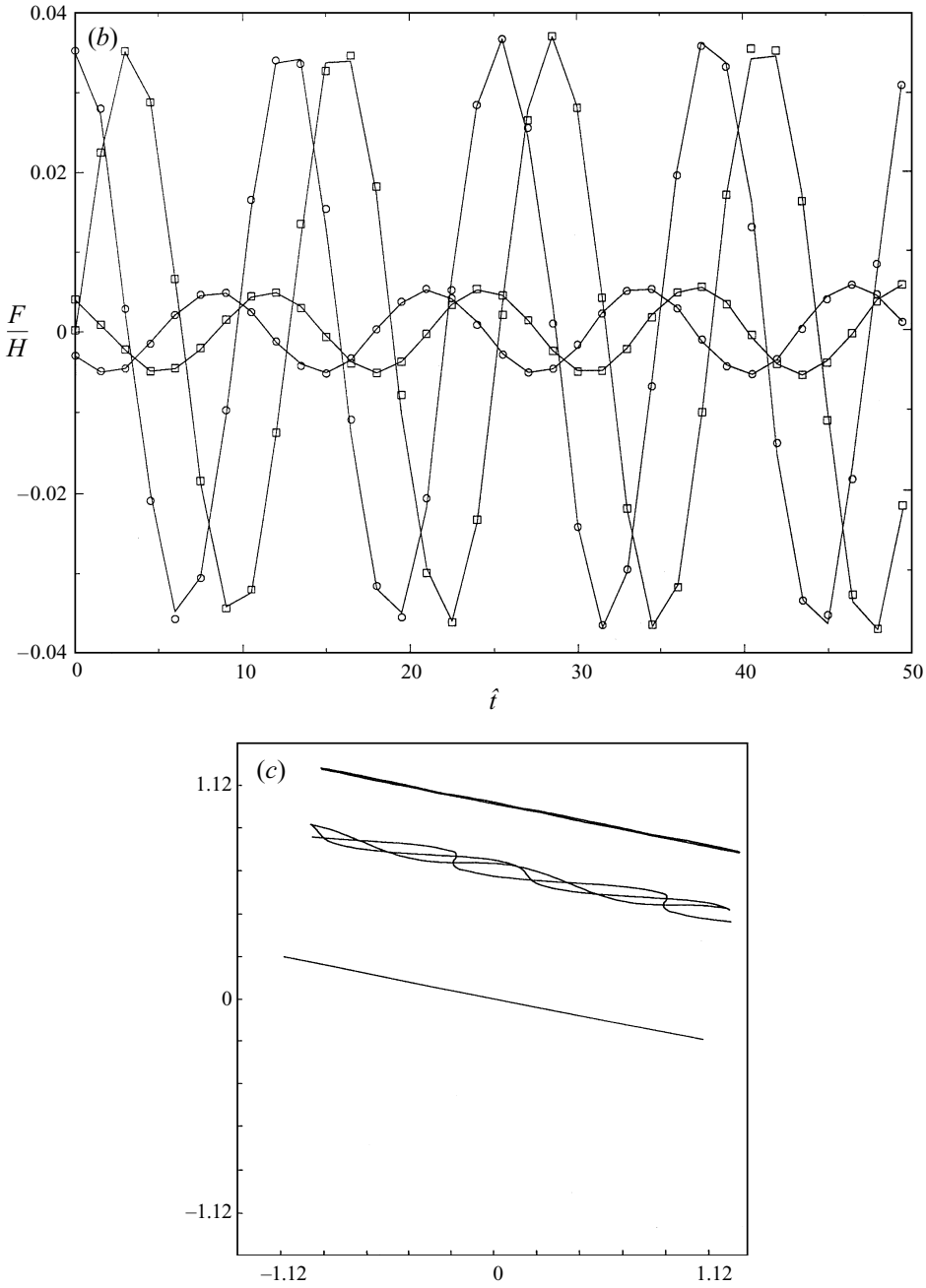


FIGURE 7. Two-film flow. (*a*) Evolution of the Fourier coefficients $F_{j,c}(t)$, $F_{j,s}(t)$ subject to an arbitrary small-amplitude perturbation for the conditions described in the text, plotted against the reduced time $\hat{t} \equiv t\rho_1 gH/\mu_1$; the curves with the large-amplitude oscillations correspond to the interface, and those with the small-amplitude oscillations correspond to the free surface; the symbols represent the results of Prony's method; circles and diamonds are for the cosine coefficients, squares and triangles are for the sine coefficients. (*b*) Same as in (*a*), but for a disturbance nearly corresponding to the unstable normal mode. (*c*) Three stages in the evolution of the flow corresponding to (*b*), after the interfacial wave has grown to a large amplitude.

https://doi.org/10.1017/S0022112098002213 Published online by Cambridge University Press

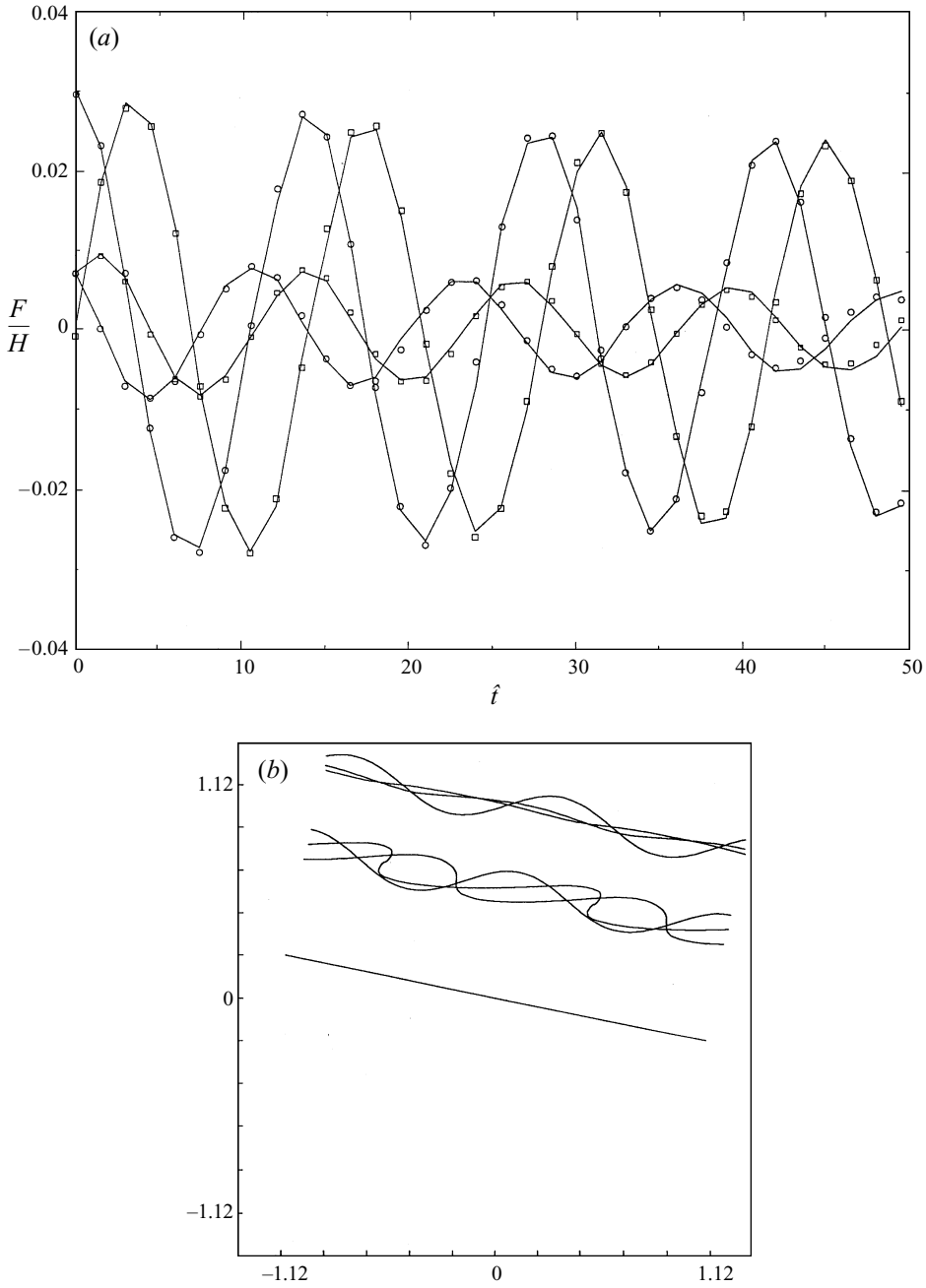


FIGURE 8. Effect of interfacial tension on the stability of two-film flow. (*a*) Evolution of the Fourier coefficients $F_{j,c}(t)$, $F_{j,s}(t)$ subject to an arbitrary small-amplitude perturbations for the conditions described in the text; the curves and symbols have the meaning as for figure 7. (*b*) Initial and evolving profiles for a large-amplitude perturbation.

8(*a*), we plot the Fourier coefficients of the interface and free-surface waves; the symbols indicate the Prony fitting with sampling time $\Delta t = 1.5\,\mu_1/(\rho_1 gH)$. The results show that the waves decay with a dimensionless rate of decay $\hat{\sigma}_I^{NM,1}$ that is close to

https://doi.org/10.1017/S0022112098002213 Published online by Cambridge University Press

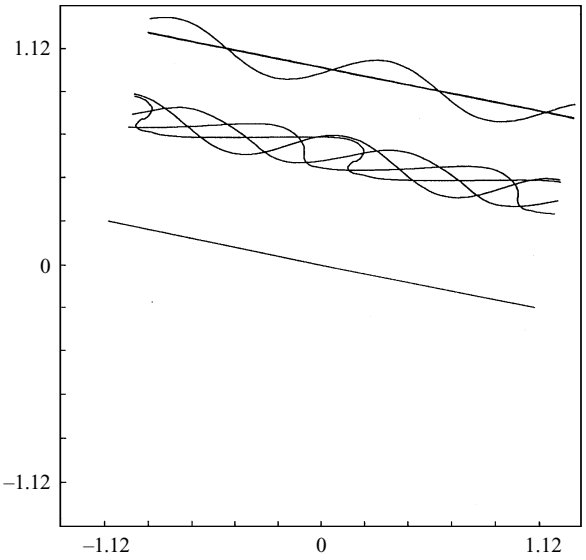


FIGURE 9. Effect of free-surface tension on the stability of two-film flow. Initial and evolving profiles subject to an arbitrary perturbation for the conditions described in the text.

-0.005, while propagating with a phase velocity corresponding to the real part of a dimensionless growth rate $\hat{\sigma}_R^{NM,1}$ that is close to 0.45. The graph in figure 5 of Chen (1993) shows the linear rate $\hat{\sigma}_I^{NM,1} = -0.0035$ which is in fair agreement with that deduced from the simulations. It is striking that a slight amount of surface tension is able to stabilize the flow. Increasing the amplitude of the perturbation leads to the permanent deformation for this linearly stable flow. This is exemplified in figure 8(*b*) where we present evolving profiles for $A_1/H = 0.10$, $A_2/H = 0.10$, keeping all other parameters constant, up to the point where the simulation is no longer reliable. The formation of penetrating lobes is a familiar feature of the motion.

As a last topic, we consider the effect of free-surface tension γ_2 expressed by the second capillary number Ca_2 for vanishing interfacial tension, $Ca_1 = \infty$. These conditions are relevant to photographic coating technology where the fluids are typically miscible and the tension of the interface is negligible compared to that of the free surface. Linear stability analysis predicts that increasing γ_2, and thus diminishing the ability of the free surface to deform, reduces the growth rate of an unstable perturbation especially at moderate and small wavelengths. But no finite amount free-surface tension is able to stabilize a linear unstable flow, especially for long wavelengths. These predictions are confirmed by the results of the simulations.

A dramatic illustration of how the free-surface wave may decay while the interface may continue to deform and attempt to overturn is shown in figure 9 for a flow with $\theta_0 = 0.06366\pi = 0.2$, $R = 0.75$, $\lambda = 2.5$, $\beta = 1$, $Ca_1 = \infty$, and $Ca_2 = 0.498$, and a perturbation with $L/H = 1.117$ or $\alpha = 3.21$, $A_1/H = 0.10$, $A_2/H = 0.10$, $\phi_1 = 0$, $\phi_2 = 0.25\pi$. At long times, we obtain a configuration with a nearly flat free surface and a highly deformed interface, which might give the erroneous impression that the presence of the free surface is irrelevant or secondary. The evolution illustrated in figure 9 is physically accurate as long as the rate of diffusion of the two fluids into each other is smaller than the growth rate of the instability, otherwise interface smearing attenuates the viscosity contrast and decelerates the growth of the waves.

https://doi.org/10.1017/S0022112098002213 Published online by Cambridge University Press

4. Discussion

In the context of linear theory and under conditions of Stokes flow, interfacial waves in two-layer channel flow are either stable or neutrally stable, but the numerical simulations show that even moderate-amplitude perturbations may lead to permanent deformation. The two-film flow is only conditionally stable according to linear theory; but even when it is stable, moderate-amplitude perturbations may also lead to permanent deformation. The morphology of the developing interfacial patterns in channel flow is similar to that in film flow, and this suggests a common origin for the unidentified physical mechanisms responsible for large-amplitude deformations.

Considering the predictions of linear stability theory, we draw the discontinuous profile of the viscosity in channel and film flow – in the second case with the viscosity of the ambient fluid set equal to zero – smooth out the discontinuities, and make the following observations: two-layer channel flow is stable or neutrally stable; three-layer channel flow can be unstable; two-film flow can be unstable when the viscosity of the fluid next to the wall is less than that of the top fluid; multi-film flows can be unstable. These observations suggest that a necessary condition for instability under conditions of Stokes flow is that the viscosity profile attains an extreme at some point between the boundaries of the flow; further analysis is required to affirm or dismiss this conjecture.

We discussed the implementation of Prony's method for a physical system that is described by two normal modes, but the extension to higher-order systems described by p normal modes is straightforward. In the general case, the right-hand side of equations (3.9) consists of a linear combination of p complex exponentials added to their complex conjugates (Pozrikidis 1999). An approximate analysis of a system with an infinite number of normal modes may be conducted by retaining a finite number of nodes, and then using the Prony fitting to compute the growth rates on the basis of a time series. This approach, which is an alternative to formulating and then solving a standard or generalized eigenvalue problem, should be preferable when a time series of a flow variable can be readily generated by measurement of computation. Preliminary investigations with Matheu's equation suggested that the Prony method is a viable alternative to the Floquet method for assessing the stability of solutions of linear differential equations.

I am indebted to Professor Bhaskar D. Rao for bringing to my attention Prony's method. This research was supported by the National Science Foundation and the SUN Microsystems Corporation. Acknowledgement is made to the Donors of the Petroleum Research Fund, administered by the American Chemical Society, for partial support.

Appendix A. Lubrication model for two-layer flow in a channel

Consider the flow of two layers through the inclined channel confined between two parallel plates separated by the distance $2H$, as depicted in figure 1(a). The flow is driven partly by the parallel translation of the lower and upper walls along the x axis with velocities U_1 and U_2, partly by a mean pressure gradient, and partly by a constant body-force field due to gravity. In this Appendix, we present an approximate theory that models the evolution of interfacial waves whose period is long compared to the channel width, working under the auspices of the lubrication theory in the spirit of Ooms *et al.* (1985). The case of Couette and pressure-driven flow was considered earlier (Pozrikidis 1997*c*) with some variations.

https://doi.org/10.1017/S0022112098002213 Published online by Cambridge University Press

We begin by describing the interface by the equation $y = y_I(x,t)$, and then assume that the flow within each layer is locally unidirectional and the streamwise velocity profile is given by

$$u^{(1)} = -\frac{1}{2\mu_1}\left(-\frac{\partial p_1^{mod}}{\partial x}+\rho_1 g\sin\theta_0\right)(y-y_I)^2+\xi_1(y-y_I)+u_I \quad \text{for} \quad y < y_I(x,t), \tag{A 1a}$$

and

$$u^{(2)} = -\frac{1}{2\mu_2}\left(-\frac{\partial p_2^{mod}}{\partial x}+\rho_2 g\sin\theta_0\right)(y-y_I)^2+\xi_2(y-y_I)+u_I \quad \text{for} \quad y > y_I(x,t), \tag{A 1b}$$

where $p_1^{mod}(x,t)$ and $p_2^{mod}(x,t)$ are the modified pressures including hydrostatic variations due to gravity, and $\xi_1(x,t)$ and $\xi_2(x,t)$ are the shear rates of the lower or upper fluid, $\partial u/\partial x$, evaluated at the interface. Requiring the no-slip boundary condition at the walls, we set $u^{(1)}(y=-H)=U_1$ and $u^{(2)}(y=H)=U_2$, and find

$$\xi_1 = -\left(-\frac{\partial p_1^{mod}}{\partial x}+\rho_1 g\sin\theta_0\right)\frac{h_1}{2\mu_1}+\frac{u_I-U_1}{h_1}, \tag{A 2a}$$

$$\xi_2 = \left(-\frac{\partial p_2^{mod}}{\partial x}+\rho_2 g\sin\theta_0\right)\frac{h_2}{2\mu_2}-\frac{u_I-U_2}{h_2}, \tag{A 2b}$$

where $h_1(x,t)$, $h_2(x,t)$ are the local and instantaneous lower or upper layer thicknesses. To compute the interfacial velocity, we substitute the right-hand sides of equations (A 2*a*, *b*) into the equation $\mu_1\xi_1(x,t)=\mu_2\xi_2(x,t)$ expressing continuity of shear stress, and find

$$u_I = \frac{1}{2\mu_1}\frac{h_1h_2}{\lambda+r}\left[-\frac{\partial p_1^{mod}}{\partial x}-\frac{\partial p_2^{mod}}{\partial x}r+\rho_1(1+\beta r)g\sin\theta_0\right]+\frac{rU_1+\lambda U_2}{r+\lambda}, \tag{A 3}$$

where

$$r(x,t) \equiv h_2(x,t)/h_1(x,t) \tag{A 4}$$

is the local and instantaneous layer thickness ratio, $\lambda=\mu_2/\mu_1$, and $\beta=\rho_2/\rho_1$.

Requiring further that the normal stress undergo a jump across the interface, and relating this jump to the magnitude of the surface tension, we write

$$p_2^{mod} = p_1^{mod}-\rho_1 g(1-\beta)h_1\cos\theta_0+\gamma\frac{\partial^2 h_1}{\partial x^2}. \tag{A 5}$$

Using this equation to eliminate p_2^{mod} from equation (A 3), we obtain

$$u_I = \frac{1}{\lambda+r}\left[hh_2\frac{1}{\mu_1}\left(-\frac{\partial p_1^{mod}}{\partial x}+\rho_1 g\frac{1+\beta r}{1+r}\sin\theta_0\right)\right.$$
$$\left.+\frac{1}{2}\frac{h_2^2}{\mu_1}\left(\rho_1(1-\beta)g\cos\theta_0\frac{\partial h_1}{\partial x}-\gamma\frac{\partial^3 h_1}{\partial x^3}\right)\right]+\frac{rU_1+\lambda U_2}{\lambda+r}. \tag{A 6}$$

As a check, we confirm that when $U_1=0$, $U_2=0$, $r(x,t)=R$ is constant, corresponding to unidirectional flow, and $\partial p_1^{mod}/\partial x=0$, equation (A 6) reduces to equation (2.3).

https://doi.org/10.1017/S0022112098002213 Published online by Cambridge University Press

To derive an evolution equation for the interface, we integrate both sides of (A 1 *a*, *b*) with respect to y over their respective domain of definition, and find the following expressions for the flow rates:

$$Q_1 = -\left(-\frac{\partial p_1^{mod}}{\partial x} + \rho_1 g \sin\theta_0\right)\frac{h_1^3}{6\mu_1} - \tfrac{1}{2}\xi_1 h_1^2 + u_I h_1, \tag{A 7a}$$

$$Q_2 = -\left(-\frac{\partial p_2^{mod}}{\partial x} + \rho_2 g \sin\theta_0\right)\frac{h_2^3}{6\mu_2} + \tfrac{1}{2}\xi_2 h_2^2 + u_I h_2. \tag{A 7b}$$

Using equations (A 2 *a*, *b*) to eliminate $\xi_1(x,t)$ and $\xi_2(x,t)$ from (A 7 *a*, *b*), we obtain the following alternative expressions in terms of the interfacial velocity:

$$Q_1 = \left(-\frac{\partial p_1^{mod}}{\partial x} + \rho_1 g \sin\theta_0\right)\frac{h_1^3}{12\mu_1} + \tfrac{1}{2}(u_I + U_1) h_1 \tag{A 8a}$$

and

$$Q_2 = \left(-\frac{\partial p_2^{mod}}{\partial x} + \rho_2 g \sin\theta_0\right)\frac{h_2^3}{12\mu_2} + \tfrac{1}{2}(u_I + U_2) h_2. \tag{A 8b}$$

Conservation of mass requires

$$\frac{\partial h_1}{\partial t} = -\frac{\partial Q_1}{\partial x}, \quad \frac{\partial h_2}{\partial t} = -\frac{\partial Q_2}{\partial x}, \tag{A 9a, b}$$

and since $h_1 + h_2 = 2H$ is constant

$$\frac{\partial Q_1}{\partial x} = -\frac{\partial Q_2}{\partial x}. \tag{A 10}$$

Integrating equation (A 10) with respect to x, substituting expressions (A 8 *a*, *b*) for the flow rates into the resulting equation, using the interfacial condition (A 5) to eliminate p_2^{mod}, substituting the right-hand side of (A 6) in place of u_I, and then carrying out a fair amount of algebra produces the relation

$$\left(\lambda h_1^3 + h_2^3 + 12\frac{\lambda}{\lambda + r} H^2 h_2\right)\frac{1}{\mu_1}\frac{\partial p_1^{mod}}{\partial x} = \frac{\rho_1(1-\beta) g \cos\theta_0}{\mu_1}\left(h_2 + 6\frac{\lambda}{\lambda + r} H\right) h_2^2 \frac{\partial h_1}{\partial x}$$
$$-\frac{\gamma}{\mu_1}\left(h_2 + 6\frac{\lambda}{\lambda + r} H\right) h_2^2 \frac{\partial^3 h_1}{\partial x^3} + \frac{g\rho_1 \sin\theta_0}{\mu_1}\left(\lambda h_1^3 + \beta h_2^3 + 12\frac{\lambda}{\lambda + r}\frac{1 + \beta r}{1 + r} H^2 h_2\right)$$
$$+ 12\lambda H\left(\frac{r U_2 + U_1}{r + 1} + \frac{\lambda U_2 + r U_1}{\lambda + r}\right) + f(t). \tag{A 11}$$

The function $f(t)$ is evaluated by specifying the modified pressure drop over one period along each layer, $\Delta p_1^{mod} = \Delta p_2^{mod} = p_1^{mod}(x + L, t) - p_1^{mod}(x, t)$. For shear- or gravity-driven flow, $\Delta p_1^{mod} = 0$, whereas for pressure-driven flow Δp_1^{mod} is a non-zero constant.

Solving equation (A 11) for $\partial p_1^{mod}/\partial x$, substituting the result into equations (A 6) and (A 7 *a*), and then putting the resulting expression for the flow rate into equation (A 9 *a*), gives a nonlinear evolution equation for the interface position, which can be expressed in the symbolic form

$$\frac{\partial y_I}{\partial t} = -\frac{\partial Q_1}{\partial x} \equiv F\left(y_I, \frac{\partial y_I}{\partial x}, \frac{\partial^2 y_I}{\partial x^2}, \frac{\partial^3 y_I}{\partial x^3}, \frac{\partial^4 y_I}{\partial x^4}\right). \tag{A 12}$$

https://doi.org/10.1017/S0022112098002213 Published online by Cambridge University Press

The right-hand side is a strongly nonlinear function of the arguments of the function F. When the amplitude of the perturbation is small compared to the wavelength, and the surface tension is sufficiently high, equation (A 12) reduces to the standard Kuramoto–Sivashinsky equation, as shown, for example, by Charru & Fabre (1994, §IV).

To generate solutions to equation (A 12), we implemented an Euler-explicit and an Euler-implicit finite-difference method. In both methods, all spatial derivatives required for the computation of Q_1 were evaluated by centred differences, whereas $\partial Q_1/\partial x$ was computed using either central or backward (upwind) differences. The performance of the centred-difference method is discussed by Pozrikidis (1997*c*), and examples were presented in §2 of this paper. Briefly, upwind differencing is effective in describing the development and propagation of steep profiles, by suppressing the growth of spurious oscillations, but the numerical diffusivity may have a significant effect on the accuracy of the solution.

Appendix B. Boundary-integral formulation for multi-film flow down an inclined plane

Consider the gravity-driven flow of N superposed liquid films down an inclined plane, as depicted in figure 6. The film numbered 1 is adjacent to the plane, and the film numbered N is exposed to the constant ambient pressure. The first interface is adjacent to the plane, and the Nth interface is a free surface. The density and viscosity of the ith fluid are noted by $\rho_i\,\mu_i$, with the understanding that $\mu_{N+1}=0$ and $\rho_{N+1}=0$, and the surface tension of the ith interface is denoted by γ_i. All flow variables and interface profiles are repeated periodically in the x-direction with period L. In this Appendix, we present and discuss an integral equation for the fluid velocity over the interfaces and the free surface.

As a preliminary, we introduce the periodic Green's function of two-dimensional Stokes flow in a semi-infinite domain that is bounded by a plane wall, $\boldsymbol{G}^{1P-W}(\boldsymbol{x},\boldsymbol{x}_0)$, and its associated stress tensor $\boldsymbol{T}^{1P-W}(\boldsymbol{x},\boldsymbol{x}_0)$. Closed-forms expressions for these tensors are given by Pozrikidis (1992), and a FORTRAN subroutine that evaluates them is available on request. The four scalar components of $\boldsymbol{G}^{1P-W}(\boldsymbol{x},\boldsymbol{x}_0)$ represent the velocity at the point $\boldsymbol{x}$ induced by a periodic array of point forces deployed along the x-axis above the plane wall, and separated by the distance L; one of the point forces is located at the point $\boldsymbol{x}_0$. As the observation point $\boldsymbol{x}$ moves away from the wall, all components of $\boldsymbol{G}^{1P-W}(\boldsymbol{x},\boldsymbol{x}_0)$ and $\boldsymbol{T}^{1P-W}(\boldsymbol{x},\boldsymbol{x}_0)$ tend to vanish, except for $G_{xx}^{1P-W}(\boldsymbol{x},\boldsymbol{x}_0)$ that tends to a constant value depending on the distance of the point forces from the wall. As the point forces approach the wall, this constant value tends to vanish.

As a second preliminary, we decompose the velocity and pressure within the ith film into a reference and a disturbance component, denoted by the superscripts R and D, writing $\boldsymbol{u}^{(i)}=\boldsymbol{u}^{R(i)}+\boldsymbol{u}^{D(i)}$, and $p^{(i)}=p^{R(i)}+p^{D(i)}$. The reference pressure is constant and equal to the ambient pressure, and the reference velocity is defined as

$$\boldsymbol{u}^{R(i)}=\frac{\rho_i\,g\sin\theta_0}{\mu_i}\,y(2H-y)\,\boldsymbol{e}_x, \tag{B 1}$$

where H is the total film thickness in rectilinear flow, and $\boldsymbol{e}_x$ is the unit vector along the x-axis. Note that the reference velocities are related by $\boldsymbol{u}^{R(i)}=(\mu_k/\mu_i)(\rho_i/\rho_k)\,\boldsymbol{u}^{R(k)}$.

Following standard methodology, we find that for a point $\boldsymbol{x}_0$ that lies in the mth interface, $m=1,\ldots,N$, the fluid velocity satisfies the integral equation

https://doi.org/10.1017/S0022112098002213 Published online by Cambridge University Press

$$u_j^{(m)}(\boldsymbol{x}_0) = \frac{1+\beta_m}{1+\lambda_m} u_j^{R(m)}(\boldsymbol{x}_0) - \frac{1}{4\pi\mu_m}\frac{2}{1+\lambda_m}\sum_{l=1}^{N}\int_{I_l} (\Delta f_i^{(l)} - \Delta f_i^{R(l)})(\boldsymbol{x})\, G_{ij}^{1P-W}(\boldsymbol{x},\boldsymbol{x}_0)\,\mathrm{d}l(\boldsymbol{x})$$

$$+\frac{1}{2\pi\mu_m}\frac{1}{1+\lambda_m}\sum_{l=1}^{N}\mu_1\int_{I_l}^{PV}((1-\lambda_l)\,u_i(\boldsymbol{x})-(1-\beta_l)\,u_i^{R(l)}(\boldsymbol{x}))\,T_{ijk}^{1P-W}(\boldsymbol{x},\boldsymbol{x}_0)\,n_k(\boldsymbol{x})\,\mathrm{d}l(\boldsymbol{x}) \tag{B 2}$$

subject to the following definitions: $\lambda_i = \mu_{i+1}/\mu_i$ and $\beta_i = \rho_{i+1}/\rho_i$ are viscosity and density ratios, with the understanding that $\lambda_N = 0$ and $\beta_{N+1} = 0$; I_l denotes one period of the lth interface; the unit vector $\boldsymbol{n}$ is normal to the lth interface and points into the lth layer; $\Delta\boldsymbol{f}^{(l)} = \gamma_l\,\kappa^{(l)}\boldsymbol{n}^{(l)}$ is the jump in the traction across the lth interface; $\kappa^{(l)}$ is the curvature of the trace of the lth interface in the (x,y)-plane; $\Delta\boldsymbol{f}^{R(l)}$ is the jump in the traction across the lth interface of the reference flows, given by

$$\Delta\boldsymbol{f}^{R(l)} = -\rho_l(1-\beta_l)\,(y-H)\begin{bmatrix} n_x^{(l)}g_y + n_y^{(l)}g_x \\ n_x^{(l)}g_x + n_y^{(l)}g_y \end{bmatrix}. \tag{B 3}$$

The qualifier PV, signifying the principal value of the double-layer potential, applies only when $l = m$. Writing equation (B 2) for $m = 1, \ldots, N$, provides us with a system of linear Fredholm integral equations of the second kind for the interfacial velocities.

To describe the flow of a single film, we set $N = 1$, $\lambda_1 = 0$ and $\beta_1 = 0$, and obtain the following integral equation for the disturbance velocity:

$$u_j^D(\boldsymbol{x}_0) = -\frac{1}{2\pi\mu}\int_{I_1} (\Delta f_i^{(l)} - \Delta f_i^{R})(\boldsymbol{x})\, G_{ij}^{1P-W}(\boldsymbol{x},\boldsymbol{x}_0)\,\mathrm{d}l(\boldsymbol{x})$$

$$+\frac{1}{2\pi}\int_{I_1}^{PV} u_i^D(\boldsymbol{x})\, T_{ijk}^{1P-W}(\boldsymbol{x},\boldsymbol{x}_0)\, n_k(\boldsymbol{x})\,\mathrm{d}l(\boldsymbol{x}). \tag{B 4}$$

This equation was presented earlier by Pozrikidis (1997*b*; equation (2.4) with $\alpha = 2$, $\beta = 1$, and without the last deflation term), but its properties were not discussed in any detail.

In practice, we want to solve equation (B 2) by the method of successive substitutions. To assess the feasibility of doing so, we introduce the associated generalized homogeneous equation

$$\phi_j^{(m)}(\boldsymbol{x}_0) = \frac{\omega^*}{2\pi}\frac{1}{1+\lambda_m}\sum_{l=1}^{N}\frac{\mu_l}{\mu_m}(1-\lambda_l)\int_{I_l}^{PV}\phi_i(\boldsymbol{x})\, T_{ijk}^{1P-W}(\boldsymbol{x},\boldsymbol{x}_0)\, n_k(\boldsymbol{x})\,\mathrm{d}l(\boldsymbol{x}) \tag{B 5}$$

and its adjoint equation

$$\psi_j^{(m)}(\boldsymbol{x}_0) = \frac{\omega}{2\pi}\frac{1}{1+\lambda_m}\sum_{l=1}^{N}\frac{\mu_l}{\mu_m}(1-\lambda_l)\, n_k^{(l)}(\boldsymbol{x}_0)\int_{I_l}^{PV}\psi_i(\boldsymbol{x})\, T_{jik}^{1P-W}(\boldsymbol{x}_0,\boldsymbol{x})\,\mathrm{d}l(\boldsymbol{x}) \tag{B 6}$$

and investigate their spectrum of eigenvalues ω; ϕ and ψ are eigenfunctions, and an asterisk designates the complex conjugate. Note that, when $m = l = N$, the coefficients in front of the integrals in the sum on the right-hand sides of equations (B 5) and (B 6) become equal to unity.

We begin the search for the eigenvalues by considering the flow of a homogenous fluid with viscosity μ_N, where the velocity field is given by the single-layer potential:

$$w_j(\boldsymbol{x}_0) = \frac{1}{2\pi\mu_N}\sum_{l=1}^{N}\frac{\mu_l}{\mu_N}(1-\lambda_l)\int_{I_l} G_{ji}^{1P-W}(\boldsymbol{x}_0,\boldsymbol{x})\,\psi_i(\boldsymbol{x})\,\mathrm{d}l(\boldsymbol{x}). \tag{B 7}$$

https://doi.org/10.1017/S0022112098002213 Published online by Cambridge University Press

Far from the wall, the velocity $\boldsymbol{w}$ tends to become uniform and parallel to the wall. The traction on the lower or upper side of the mth interface, designated by a plus or a minus sign, is given by

$$f_j^{\pm}(\boldsymbol{x}_0) = \mp\frac{\mu_m}{\mu_N}(1-\lambda_m)\,\psi_j(\boldsymbol{x}_0)+\frac{1}{2\pi}\sum_{l=1}^{N}\frac{\mu_l}{\mu_N}(1-\lambda_l)\,n_k(\boldsymbol{x}_0)\int_{I_l}^{PV} T_{jik}^{1P-W}(\boldsymbol{x}_0,\boldsymbol{x})\,\psi_i(\boldsymbol{x})\,\mathrm{d}l(\boldsymbol{x}), \tag{B 8}$$

where the point $\boldsymbol{x}_0$ lies at the mth interface, the unit normal vector $\boldsymbol{n}$ points into the mth film, and the qualifier PV applies only when $l = m$. Combining equations (B 6) and (B 8) to eliminate the sum, we find

$$f_j^{\pm}(\boldsymbol{x}_0) = \frac{\mu_m}{\mu_N}\left(\frac{1+\lambda_m}{\omega}\mp(1-\lambda_m)\right)\psi_j(\boldsymbol{x}_0). \tag{B 9}$$

The rate of energy dissipation of the flow $\boldsymbol{w}$ within the first layer L_1 is given by

$$D^{(1)} \equiv 2\mu_N\int_{L_1} e_{ik}\,e_{ik}^*\,\mathrm{d}A = -\int_{I_1} w_i^* f_i^+\,\mathrm{d}A, \tag{B 10a}$$

where $\boldsymbol{e}$ is the rate of deformation tensor. The rate of energy dissipation within the subsequent layers L_j is given by

$$D^{(j)} \equiv 2\mu_N\int_{L_j} e_{ik}\,e_{ik}^*\,\mathrm{d}A = \int_{I_{j-1}} w_i^* f_i^-\,\mathrm{d}A-\int_{I_j} w_i^* f_i^+\,\mathrm{d}A \tag{B 10b}$$

for $j = 1, \ldots, N$. And the rate of dissipation within the semi-infinite region above the top layer, denoted as L_{N+1}, is given by

$$D^{(N+1)} \equiv 2\mu_N\int_{L_{N+1}} e_{ik}\,e_{ik}^*\,\mathrm{d}A = \int_{I_N} w_i^* f_i^-\,\mathrm{d}A. \tag{B 10c}$$

Next, we define the projection

$$P^{(j)} \equiv \frac{1}{\mu_N}\int_{I_j} w_i^*\,\psi_i\,\mathrm{d}A, \tag{B 11}$$

where $\boldsymbol{P}^{(0)} = 0$ because $\boldsymbol{w}$ vanishes on the wall, and combine equations (B 9) and (B 10) to find

$$D^{(1)} = \mu_1\left(-\frac{1+\lambda_1}{\omega}+1-\lambda_1\right)P^{(1)}, \tag{B 12a}$$

$$D^{(j)} = \mu_{j-1}\left(\frac{1+\lambda_{j-1}}{\omega}+1-\lambda_{j-1}\right)P^{(j-1)}+\mu_j\left(-\frac{1+\lambda_j}{\omega}+1-\lambda_j\right)P^{(j)}, \tag{B 12b}$$

for $j = 2, \ldots, N$, when $N > 1$, and

$$D^{(N+1)} = \mu_N\left(\frac{1}{\omega}+1\right)P^{(N)}. \tag{B 12c}$$

To study the spectrum of eigenvalues, we successively eliminate the projections $P^{(j)}$ among equations (B 12a–c), starting from the top or bottom, and thus obtain a polynomial equation for ω whose degree is equal to the number of layers, N. The polynomial coefficients involve the real and non-negative dissipation integrals $D^{(j)}$.

https://doi.org/10.1017/S0022112098002213 Published online by Cambridge University Press

Unfortunately, it was not possible to derive general results on the location of the eigenvalues, except in the case of one layer considered in the next subsection. The most general remark we are able to make is that $\omega = -1$ is a double eigenvalue; the associated eigenfunctions over the free surface are equal to those described next for single-layer flow, and vanish over the interfaces. These eigenvalues may be removed by the method of Weilandt deflation, as will be described next for single-layer flow. In practice, we found that, with deflation implemented, the method of successive substitutions for two-film flow converges rapidly for a broad range of viscosity ratios.

One layer

In the case of one layer, $N = 1, \lambda_1 = 0$, equations (B 5) and (B 6) simplify to

$$\phi_j(\boldsymbol{x}_0) = \frac{\omega^*}{2\pi} \int_{I_1}^{PV} \phi_i(\boldsymbol{x})\, T_{ijk}^{1P-W}(\boldsymbol{x}, \boldsymbol{x}_0)\, n_k(\boldsymbol{x})\, \mathrm{d}l(\boldsymbol{x}) \tag{B 13}$$

and

$$\psi_j(\boldsymbol{x}_0) = \frac{\omega}{2\pi} n_k(\boldsymbol{x}_0) \int_{I_1}^{PV} \psi_i(\boldsymbol{x})\, T_{jik}^{1P-W}(\boldsymbol{x}_0, \boldsymbol{x})\, \mathrm{d}l(\boldsymbol{x}). \tag{B 14}$$

For simplicity, we have omitted the superscripts indicating the interface number. Using equations (B 12a) and (B 12c), we find

$$D^{(1)} = \mu_1 \left(-\frac{1}{\omega} + 1 \right) P^{(1)}, \quad D^{(2)} = \mu_1 \left(\frac{1}{\omega} + 1 \right) P^{(1)}. \tag{B 15a,b}$$

Dividing corresponding sides to eliminate $P^{(1)}$ yields a linear equation for ω whose solution is $\omega = (1+\delta)/(1-\delta)$ with $\delta \equiv D^{(1)}/D^{(2)}$. Since $D^{(1)}$, $D^{(2)}$, and thus δ is real and non-negative, ω lies outside the closed interval $[-1, 1]$. This result, however, presumes that neither $D^{(1)}$ nor $D^{(2)}$ is equal to zero.

The vanishing of $D^{(1)}$ demands that the velocity $\boldsymbol{w}$ within the layer express rigid-body motion, which is prevented by the requirement that $\boldsymbol{w}$ takes zero values over the wall. We may still have $\boldsymbol{f}^+ = c\boldsymbol{n}$ where c is an arbitrary constant, in which case equation (B 9) with $m = 1$ and $\lambda_1 = 0$ yields $\boldsymbol{\psi} = c\boldsymbol{n}\omega/(1-\omega)$. Substituting this expression into equation (B 14), and using the identity

$$\int_C^{PV} n_i(\boldsymbol{x})\, T_{jik}^{1P-W}(\boldsymbol{x}_0, \boldsymbol{x})\, \mathrm{d}l(\boldsymbol{x}) = -2\pi\delta_{ik}, \tag{B 16}$$

where C is one period of a periodic line passing through the singular point $\boldsymbol{x}_0$, we find $\omega = -1$. Note that equation (B 15b) requires that $D^{(2)} = 0$.

The vanishing of $D^{(2)}$ demands that the velocity $\boldsymbol{w}$ above the layer express rigid-body motion, but since rotation is precluded by periodicity, and translation normal to the wall is precluded by the far-field properties of the Green's function, we are left only with translation parallel to the wall. Equation (B 9) shows that ψ is proportional to the traction $\boldsymbol{f}^+$ exerted on the upper wall of a channel confined between a stationary plane lower wall and a periodic upper wall that coincides with the interface. The flow is generated by the translation of the upper wall parallel to the lower wall. Since the pressure of the fluid within the channel may be set at an arbitrary level, the traction $\boldsymbol{f}^+$ and thus $\boldsymbol{\psi}$ may be expressed as $c_1\boldsymbol{f}_{tr} + c_2\boldsymbol{n}$, where $\boldsymbol{f}_{tr}$ is any one traction, and c_1, c_2 are two arbitrary constants. We note that $P^{(1)} \neq 0$ when $\boldsymbol{\psi} = \boldsymbol{\psi}^{(1)} \equiv \boldsymbol{f}_{tr}$, and use equation (B 15$b$) to find the eigenvalue $\omega = -1$.

We thus found that $\omega = -1$ is a double eigenvalue with eigenfunctions $\boldsymbol{\psi}^{(1)} \equiv \boldsymbol{f}_{tr}$ and $\boldsymbol{\psi}^{(2)} = \boldsymbol{n}$. It should be noted that the properties of the present integral equation over a

https://doi.org/10.1017/S0022112098002213 Published online by Cambridge University Press

periodic interface deviate from those of the same integral equation defined over a closed interface. In the latter case, the eigenfunction $\boldsymbol{\psi}^{(2)}$ corresponds to the eigenvalue $\omega = 1$ instead of -1.

One may verify, using the definition of the Green's function, that the two eigenfunctions of (B 13) for $\omega = -1$, denoted as $\boldsymbol{\phi}^{(1)}$ and $\boldsymbol{\phi}^{(2)}$, represent rigid-body translation along the x- or y-axis, respectively. The adjoint eigenfunction $\boldsymbol{\psi}^{(2)} = \boldsymbol{n}$ is orthogonal to the eigenfunction $\boldsymbol{\phi}^{(1)}$, and may thus be associated with the eigenfunction $\boldsymbol{\phi}^{(2)}$. When the interface is symmetric with respect to its mid-plane over each period, and this symmetry is exploited in the implementation of the numerical method to reduce the domain of integration to half the length of the interface, the eigenfunction $\boldsymbol{\phi}^{(1)}$ and its adjoint $\boldsymbol{\psi}^{(1)}$ do not appear.

In summary, we found that the spectral radius of the double-layer operator is equal to unity, which undermines the convergence of the method of successive substitutions. To remove the eigenfunctions of the marginal eigenvalue $\omega = -1$, we apply the method of Weilandt deflation. The simplest way of removing the eigenfunction $\boldsymbol{\psi}^{(2)}$, is to add to the right-hand side of the integral equation (B 4) the deflating term

$$n_j(\boldsymbol{x}_0)\frac{1}{\Gamma_1}\int_{I_1} u_i^D(\boldsymbol{x})\, n_i(\boldsymbol{x})\, \mathrm{d}l(\boldsymbol{x}), \tag{B 17}$$

where Γ_1 is the arclength of the free surface over a period (this rectifies a typographical error in sign on the left-hand side of equations (2.3) and (2.4) of Pozrikidis 1997*a*). With this addition, $\boldsymbol{\psi}^{(2)}$ remains an eigenfunction of the associated adjoint generalized homogeneous equation, but the corresponding eigenvalue has been shifted to infinity. The eigenfunction $\boldsymbol{\phi}^{(1)}$ is still present, except when the free surface is symmetric with respect to the mid-plane, as discussed in the preceding paragraph. In that case, this partial deflation is sufficient for the method of successive substitutions to produce a convergent solution.

To achieve complete deflation, we replace $\boldsymbol{u}^D$ in equation (B 4) by the modified velocity $\boldsymbol{v}^D$, and add to the right-hand side the deflating term

$$\frac{1}{\Gamma_1}\int_{I_1} v_j^D(\boldsymbol{x})\, \mathrm{d}l(\boldsymbol{x}). \tag{B 18}$$

With this addition, $\boldsymbol{\phi}^{(1)}$ and $\boldsymbol{\phi}^{(2)}$ become eigenfunctions of the associated adjoint generalized homogeneous equation corresponding to an infinite eigenvalue, while all other eigenvalues remain unchanged. At the second stage, we solve the resulting equation by the method of successive substitutions, and recover the disturbance velocity by setting

$$u_j^D(\boldsymbol{x}_0) = v_j^D(\boldsymbol{x}_0) - \frac{1}{2}\frac{1}{\Gamma_1}\int_{I_1} v_j^D(\boldsymbol{x})\, \mathrm{d}l(\boldsymbol{x}). \tag{B 19}$$

REFERENCES

Chang, H.-C. 1994 Wave evolution on a falling film. *Ann. Rev. Fluid Mech.* **26**, 103–136.

Charru, F. & Fabre, J. 1994 Long waves at the interface between two viscous fluids. *Phys. Fluids* **6**, 1223–1235.

Chen, K. 1992 The onset of elastically driven wavy motion in the flow of two viscoelastic liquid films down an inclined plane. *J. Non-Newtonian Fluid Mech.* **45**, 21–45.

Chen, K. 1993 Wave formation in the gravity-driven low-Reynolds-number flow of two liquid films down an inclined plane. *Phys. Fluids* A **5**, 3038–3048.

https://doi.org/10.1017/S0022112098002213 Published online by Cambridge University Press

Gwynllyw, D. Rh. & Peregrine, D. H. 1996 Numerical simulation of Stokes flow down an inclined plane. *Proc. R. Soc. Lond.* A **452**, 543–565.

Han, C. D. 1981 *Multiphase Flow in Polymer Processing*. Academic.

Hildebrand, F. B. 1974 *Introduction to Numerical Analysis*. Dover.

Kay, S. M. & Marple, L. jr 1981 Spectrum analysis – a modern perspective. *Proc. IEEE* **69**, 1380–1419.

Kistler, S. F. & Schweizer, P. M. (Eds.) 1997 *Liquid Film Coating*. Chapman & Hall.

Kliakhandler, I. L. & Sivashinsky, G. I. 1997 Viscous damping and instabilities in stratified liquid film flowing down a slightly inclined plane. *Phys. Fluids* **9**, 23–30.

Kobayashi, C. 1992 Stability analysis of film flow on an inclined plane. I. One layer, two layer flow. *Indust. Coating Res.* **2**, 65–88.

Kobayashi, C. 1995 Stability analysis of film flow on an inclined plane. II. Multi-layer flow. *Indust. Coating Res.* **3**, 103–125.

Li, C.-H. 1969 Instability of three-layer viscous stratified flow. *Phys. Fluids* **12**, 2473–2481.

Loewenherz, D. S. & Lawrence, C. J. 1989 The effect of viscosity stratification on the stability of a free surface flow at low Reynolds number. *Phys. Fluids* A **1**, 1686–1693.

Marple, S. L. 1987 *Digital Spectral Analysis with Applications*. Prentice Hall.

Ooms, G., Segal, A., Cheung, S. Y. & Oliemans, R. V. A. 1985 Propagation of long waves of finite amplitude at the interface of two viscous fluids. *Intl J. Multiphase Flow* **11**, 481–502.

Pozrikidis, C. 1992 *Boundary Integral and Singularity Methods for Linearized Viscous Flow*. Cambridge University Press.

Pozrikidis, C. 1997*a* *Introduction to Theoretical and Computational Fluid Dynamics*. Oxford University Press.

Pozrikidis, C. 1997*b* Numerical studies of singularity formation at fluid interfaces in two-dimensional Stokes flow. *J. Fluid Mech.* **331**, 145–167.

Pozrikidis, C. 1997*c* Instability of two-layer creeping flow in a channel with parallel-sided walls. *J. Fluid Mech.* **351**, 139–165.

Pozrikidis, C. 1998 *Numerical Computation in Science and Engineering*. Oxford University Press.

Pozrikidis, C. 1999 Multi-film flow down an inclined plane: Simulations based on the lubrication approximation, and normal-mode decomposition of linear waves. In *Fluid Dynamics at Interfaces* (ed. W. Shyy). Cambridge University Press (in Press).

Severtson, Y. C. & Aidun, C. K. 1996 Stability of two-layer stratified flow in inclined channels: applications to air entrainment in coating systems. *J. Fluid Mech.* **312**, 173–200.

Tilley, B. S., Davis, S. H. & Bankoff, S. G. 1994*a* Linear stability theory of two-layer fluid flow in an inclined channel. *Phys. Fluids* **6**, 3906–3922.

Tilley, B. S., Davis, S. H. & Bankoff, S. G. 1994*b* Nonlinear long-wave stability of superposed fluids in an inclined channel. *J. Fluid Mech.* **277**, 55–83.

Weinstein, S. J. 1990 Wave propagation in the flow of shear-thinning fluids down an incline. *AIChE J.* **36**, 1873–1889.

Weinstein, S. J. & Kurz, M. R. 1991 Long-wavelength instabilities in three-layer flow down an incline. *Phys. Fluids* A **3**, 2680–2687.

Yiantsios, S. & Higgins, B. G. 1988 Linear stability of plane Poiseuille flow of two superposed fluids. *Phys. Fluids* **31**, 3225–3238.

Yih, C. S. 1963 Stability of liquid flow down an inclined plane. *Phys. Fluids* **6**, 321–334.

Yih, C. S. 1967 Instability due to viscosity stratification. *J. Fluid Mech.* **27**, 337–352.

https://doi.org/10.1017/S0022112098002213 Published online by Cambridge University Press